Article

Cell Reports

Small-Molecule and CRISPR Screening Converge to Reveal Receptor Tyrosine Kinase Dependencies in Pediatric Rhabdoid Tumors

Graphical Abstract

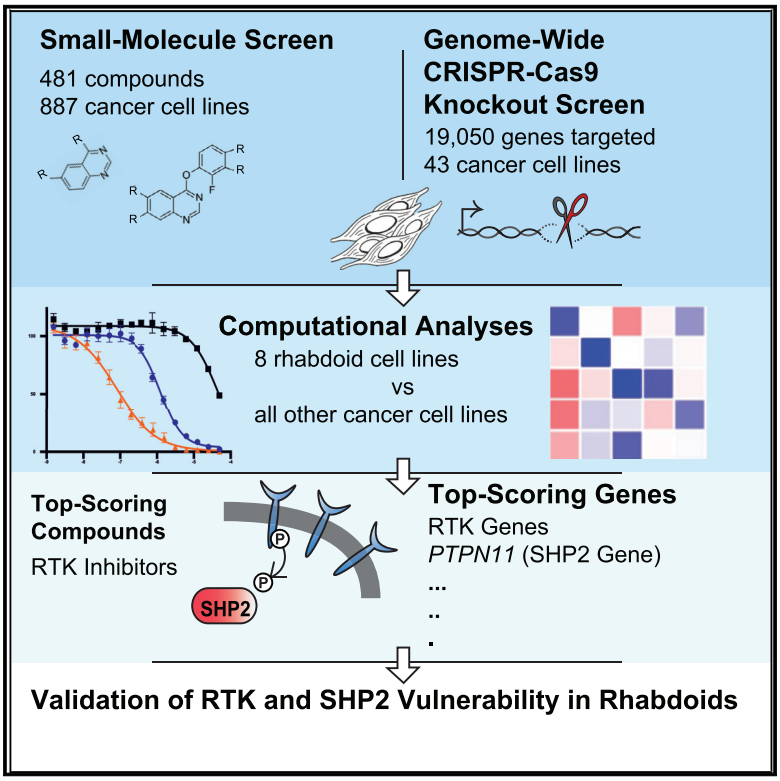

Highlights

- Rhabdoid cell lines and tumors have few mutations yet highly express a range of RTKs
- RTKs and SHP2 are vulnerabilities in small-molecule and CRISPR-knockout screens
- RTK inhibitors are effective against a xenografted rhabdoid mouse model *in vivo*
- Perturbational screens may identify vulnerabilities not detectable in genomic analyses

Authors

Elaine M. Oberlick, Matthew G. Rees, Brinton Seashore-Ludlow, ..., Elizabeth A. Stewart, Stuart L. Schreiber, Charles W.M. Roberts

Correspondence

reesm@broadinstitute.org (M.G.R.), charles.roberts@stjude.org (C.W.M.R.)

In Brief

Using a diverse set of rhabdoid tumor cell lines and both small-molecule and CRISPR-Cas9 gene-knockout screening, Oberlick et al. find high expression and dependency upon a wide range of receptor tyrosine kinases (RTKs) and SHP2 downstream. These RTK inhibitors are also effective against a rhabdoid tumor mouse model.

Oberlick et al., 2019, Cell Reports *28*, 2331–2344
August 27, 2019
https://doi.org/10.1016/j.celrep.2019.07.021

CellPress

Cell Reports
Article

Small-Molecule and CRISPR Screening Converge to Reveal Receptor Tyrosine Kinase Dependencies in Pediatric Rhabdoid Tumors

Elaine M. Oberlick,[1,2,3,14] Matthew G. Rees,[3,14,*] Brinton Seashore-Ludlow,[3,4] Francisca Vazquez,[3] Geoffrey M. Nelson,[5] Neekesh V. Dharia,[1,3,6,7] Barbara A. Weir,[3,18] Aviad Tsherniak,[3] Mahmoud Ghandi,[3] John M. Krill-Burger,[3] Robin M. Meyers,[3] Xiaofeng Wang,[1,16] Phil Montgomery,[3] David E. Root,[3] Jake M. Bieber,[3] Sandi Radko,[8] Jaime H. Cheah,[3,15] C. Suk-Yee Hon,[3] Alykhan F. Shamji,[3,17] Paul A. Clemons,[3] Peter J. Park,[5,9] Michael A. Dyer,[10] Todd R. Golub,[3,6,11] Kimberly Stegmaier,[1,3,7] William C. Hahn,[3,11,12] Elizabeth A. Stewart,[10] Stuart L. Schreiber,[3,13] and Charles W.M. Roberts[8,19,*]

[1]Department of Pediatric Oncology, Dana-Farber Cancer Institute, Boston, MA 02215, USA
[2]Biological and Biomedical Sciences Program, Harvard Medical School, Boston, MA 02115, USA
[3]Broad Institute, Cambridge, MA 02142, USA
[4]Science for Life Laboratory, Department of Oncology-Pathology, Karolinska Institute, 171 77 Stockholm, Sweden
[5]Department of Biomedical Informatics, Harvard Medical School, Boston, MA 02115, USA
[6]Department of Pediatrics, Harvard Medical School, Boston, MA 02215, USA
[7]Boston Children's Hospital, Boston, MA 02115, USA
[8]Comprehensive Cancer Center and Department of Oncology, St. Jude Children's Research Hospital, Memphis, TN 38105, USA
[9]Harvard Ludwig Center, Harvard Medical School, Boston, MA 02115, USA
[10]Department of Developmental Neurobiology, St. Jude Children's Research Hospital, Memphis, TN 38105, USA
[11]Department of Medical Oncology, Dana-Farber Cancer Institute, Boston, MA 02215, USA
[12]Department of Medicine, Brigham and Women's Hospital and Harvard Medical School, Boston, MA 02115, USA
[13]Department of Chemistry and Chemical Biology, Harvard University, Cambridge, MA 02138, USA
[14]These authors contributed equally
[15]Present address: Koch Institute for Integrative Cancer Research at MIT, Cambridge, MA 02139, USA
[16]Present address: Department of Molecular & Systems Biology, Norris Cotton Cancer Center, Geisel School of Medicine at Dartmouth College, Lebanon, NH 03756, USA
[17]Present address: Massachusetts General Hospital, Boston, MA 02114, USA
[18]Present address: Janssen R&D, Cambridge, MA 02142, USA
[19]Lead Contact
*Correspondence: reesm@broadinstitute.org (M.G.R.), charles.roberts@stjude.org (C.W.M.R.)
https://doi.org/10.1016/j.celrep.2019.07.021

SUMMARY

Cancer is often seen as a disease of mutations and chromosomal abnormalities. However, some cancers, including pediatric rhabdoid tumors (RTs), lack recurrent alterations targetable by current drugs and need alternative, informed therapeutic options. To nominate potential targets, we performed a high-throughput small-molecule screen complemented by a genome-scale CRISPR-Cas9 gene-knockout screen in a large number of RT and control cell lines. These approaches converged to reveal several receptor tyrosine kinases (RTKs) as therapeutic targets, with RTK inhibition effective in suppressing RT cell growth *in vitro* and against a xenograft model *in vivo*. RT cell lines highly express and activate (phosphorylate) different RTKs, creating dependency without mutation or amplification. Downstream of RTK signaling, we identified *PTPN11*, encoding the pro-growth signaling protein SHP2, as a shared dependency across all RT cell lines. This study demonstrates that large-scale perturbational screening can uncover vulnerabilities in cancers with "quiet" genomes.

INTRODUCTION

Large-scale perturbational screening of cancer cell lines aims to provide mechanistic insight into cancer biology and identify therapeutic vulnerabilities, which may prove especially useful for cancers that lack obvious targetable genetic alterations. Although direct targeting of activated oncogenes is now a proven therapeutic approach, mutations in tumor suppressor genes are more common across many cancer types and cannot be targeted directly (Lawrence et al., 2013). Here, we investigate the potential of large-scale perturbational screening to identify vulnerabilities in highly aggressive and lethal pediatric rhabdoid tumors (RTs). This genomically simple cancer is driven by a single recurrent genetic event: biallelic loss of the tumor suppressor *SMARCB1*, or much less commonly *SMARCA4*, core subunits of the SWI/SNF (BAF) chromatin-remodeling complex. The average mutation burden in RTs is more than 20-fold lower than the average across cancer types; recent genomic characterization of large numbers of primary patient RTs has revealed that 80% of RTs have *SMARCB1* loss as the sole recurrent

mutation (Lawrence et al., 2013; Lee et al., 2012; Roberts et al., 2000). The cell(s) of origin have been unknown, and tumors can occur in various soft tissues, including kidney, liver, or brain (these brain-localized tumors are known as AT/RT [atypical teratoid/rhabdoid tumor]). Recent data reveal at least three distinct sub-classes of RTs that may each arise from different progenitor cells (Torchia et al., 2015; Johann et al., 2016; Chun et al., 2016). The range of RT tissue origins and sub-classes complicates treatment recommendations, as dependency relationships are often unclear.

Mechanistically, we have recently demonstrated that the SWI/SNF chromatin-remodeling complex is essential for the maintenance of enhancers (Mathur et al., 2017) and that inactivation of the SMARCB1 subunit of this complex, as occurs in nearly all RTs, disrupts enhancer function, which impairs differentiation and thus may underlie unrestrained proliferation (Alver et al., 2017; Wang et al., 2017).

Given that the sole identified recurrent genetic event is the absence of a gene, there are no obvious therapeutic targets, and mortality remains high (Wang et al., 2009). Therefore, RT constitutes a compelling model with which to investigate the potential of large-scale perturbational screening of cancer cell lines to identify therapeutic vulnerabilities.

Consequently, we collected 16 RT cell-line models (derived from tumors found in brain, kidney, muscle, and soft tissue tumors) and robustly deployed both small-molecule and genetic (CRISPR-Cas9-mediated gene knockout) perturbational screening to discover vulnerabilities in RT.

These approaches converged to reveal several receptor tyrosine kinases (RTKs) as therapeutic targets in RT, with RTK inhibition effective in suppressing RT cell growth *in vitro* and against a xenograft model *in vivo*. We find that rhabdoid cell lines from all tissue origins activate a heterogeneous range of RTKs, including *PDGFRA* and *MET*, contributing to the proliferation of RT cells and leading to dependency on these pathways. Overall, we find that RTK activation, driven in part by increased expression caused by loss of *SMARCB1*, rather than genomic alterations, is a hallmark of RT model systems and that high levels of RTK expression are observed in primary RT patient samples. Both genetically and using a small-molecule inhibitor, we also find that RTK-dependent RT cells are particularly sensitive to loss of the protein tyrosine phosphatase *PTPN11* (encoding SHP2), a downstream effector of RTK signaling. These findings highlight the potential of large-scale perturbational screening to reveal dependencies conferred by tumor suppressor loss and suggest RTKs and SHP2 as therapeutic targets in patients with RT.

RESULTS

RTK Inhibitors Selectively Target RT Cell Lines

Previously, we reported a small-molecule sensitivity dataset (Cancer Therapeutics Response Portal) describing the effects of a library of 481 small molecules, an informer set enriched for U.S. Food and Drug Administration (FDA)-approved oncology drugs and clinical candidates, on the viability of 840 individual cancer cell lines (CCLs) representing 25 cancer lineages, which included 4 RT CCLs (Seashore-Ludlow et al., 2015; Rees et al., 2016). We tested 47 additional CCLs, including 5 RT CCLs, against this small-molecule collection, using area-under-concentration-response curves (AUCs) to measure sensitivity as described previously (Seashore-Ludlow et al., 2015; Rees et al., 2016). We normalized AUCs for each small molecule across all 887 CCLs by calculating a robust Z score using the median absolute deviation (ZMAD). To identify potential therapeutic vulnerabilities in these 9 RT cell lines (a diverse set derived from brain, kidney, muscle, and soft tissue tumors), we focused on small molecules selective for RT CCLs relative to non-RT CCLs. Of the 15 most selective small molecules (ZMAD AUC < -3 in at least 3 RT CCLs), 14 were annotated RTK inhibitors, targeting angiogenesis-related receptors such as vascular endothelial growth factor receptor (VEGFR), platelet-derived growth factor receptor (PDGFR), fibroblast growth factor receptor (FGFR), and hepatocyte growth factor receptor (HGFR/MET). Overall, RTK inhibitors as a class were highly selective for RT cell lines compared with non-RT cell lines, suggesting a remarkable dependence on these targets (Kolmogorov-Smirnov $p = 7.3 \times 10^{-11}$; Figure 1A; Figure S1A). The selectivity of FDA-approved RTK inhibitors for RT CCLs compared with CCLs best representing currently approved indications is presented in Figure S1B.

To expand on this finding, we collected 7 additional RT CCLs and tested all 16 validated SMARCB1-deficient RT CCLs against 30 RTK inhibitors, including FDA-approved therapeutics (Figure S1C). Results were consistent with high-throughput data and further suggested distinct vulnerabilities of sets of cell lines to sets of small molecules: different RTK inhibitors potently inhibited the viability of different subsets of RT cell lines (e.g., imatinib: G402, A204, KD, NCIH2004RT, and KPMRTRY; crizotinib: MON, TM87, TTC642, and TTC549) while showing little efficacy against others (Figure 1B; Figure S1A; Table S1). Of note, RTK inhibitors with overlapping target profiles (Table S2; Figure S1D) clustered together in these results, suggesting on-target activity.

RTKs Are Preferential Dependencies in RT CCLs

In parallel, we carried out genome-scale CRISPR-Cas9-mediated gene-knockout screens on eight RT CCLs with six guide RNAs targeting each gene (Aguirre et al., 2016; Meyers et al., 2017). Values were collapsed to a single dependency score per gene and adjusted per cell line using CERES to account for the confounding factor of copy number in CRISPR-Cas9 screens (Aguirre et al., 2016; Munoz et al., 2016), with normalization to pan-essential (score of -1) and non-essential (score of 0) genes. Notably, each RT cell line displayed a strong dependency on at least one RTK, although the specific dependencies again varied by cell line (Figure 1C; Figure S2E; Table S3). The strongest observed dependencies included *FGFR1*, *MET*, *PDGFRA*, and *PDGFRB* (CERES score ZMAD < -4 in at least two RT CCLs), while other RTKs were strong dependencies in a single RT CCL (e.g., *PDGFRB*, *FGFR2*, and *ERBB4*; Table S3).

RTKs Are Highly Expressed and Activated in RT CCLs

To nominate biomarkers for RTK dependencies, we performed RNA sequencing on RT CCLs in conjunction with the Cancer Cell Line Encyclopedia (Ghandi et al., 2019; Barretina et al., 2012). RTK-dependent RT CCLs exhibited high expression of the corresponding RTK-encoding transcript(s) relative to both

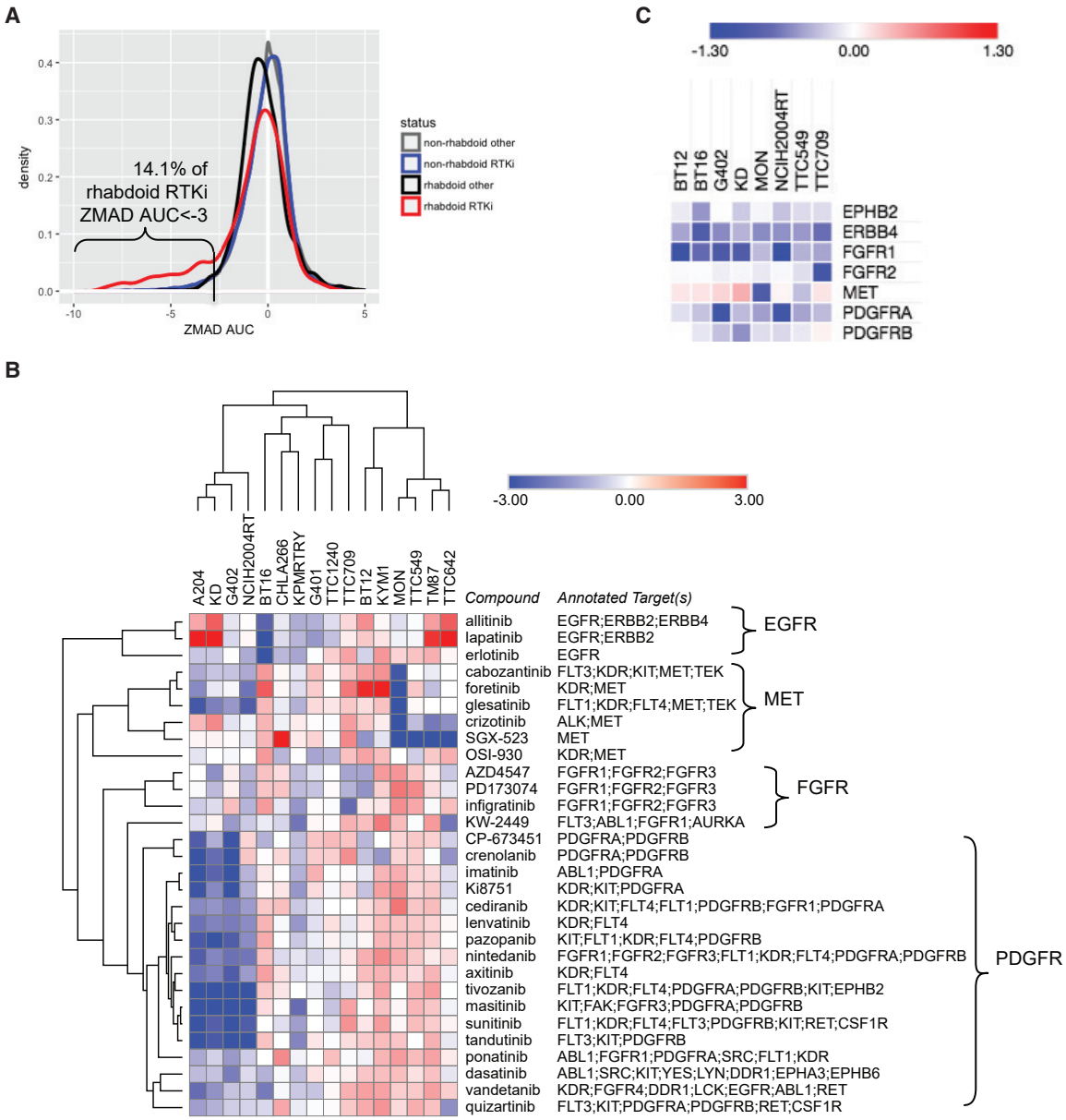

Figure 1. Receptor Tyrosine Kinases Represent Vulnerabilities within RT Cell Lines

(A) ZMAD AUC distributions for 49 annotated RTK inhibitors (and 432 non-RTK inhibitors) across 8 RT cell lines and 879 non-RT cell lines (see Figures S1A–S1C; Table S1).

(B) *Z*-scored AUC values for 30 RTK inhibitors across 16 RT CCLs (see Table S1).

(C) CERES scores for seven RTK-encoding genes with CERES scores < −0.5 and ZMAD CERES < −2 (in RT relative to 35 non-RT CCLs) in ≥1 RT CCL (see Figure S1E; Table S3). Visualization and hierarchical clustering of rows and columns (1 − Pearson correlation) were performed using Morpheus (https://software.broadinstitute.org/morpheus/).

non-dependent RT CCLs and non-RT CCLs (Figure 2A). Consistent with published primary tumor data (Chauvin et al., 2017), we see that rhabdoid cell lines have low promoter methylation at RTK genes. In the cell lines tested, we see that the same relevant dependent RTK genes have low promoter methylation, while RTKs not important in those cell lines have higher levels of promoter methylation (Figure S1F) (Ghandi et al., 2019). Measurement of total and phospho-protein levels using a global phospho-RTK array or individual antibodies demonstrated protein expression and phosphorylation (indicating activation) of the relevant RTKs in RT CCLs (Figure 2B; Figure S2A). Consistent with a contribution of *SMARCB1* in regulation of RTK activation, retroviral restoration of *SMARCB1* in the kidney RT G402 cell line reduced mRNA levels of *FGFR1* and downstream *RPS6KB1*, but not *PDGFRA* or other pathway members (Figure 2C). Both RTKs showed a decrease in activated phospho- and total protein, and

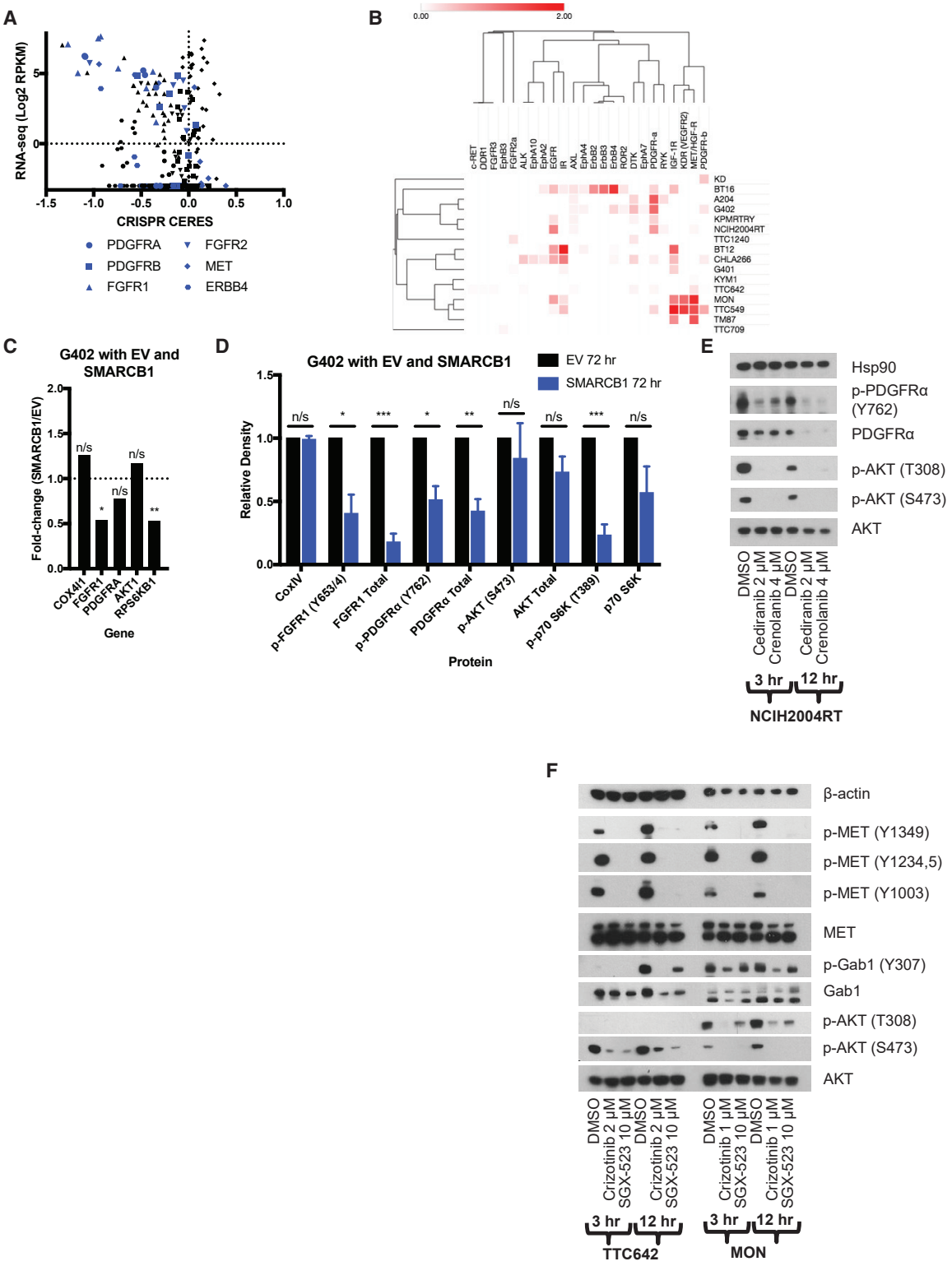

Figure 2. RT CCLs Express Activated RTKs Targetable by Small Molecules

(A) CRISPR CERES scores and RNA levels for six different RTK-encoding genes across 43 CCLs. RT CCLs are shown in blue (see Table S3).

(B) Heatmap of results of phospho-RTK array in 16 rhabdoid cell lines. Visualization and hierarchical clustering of rows and columns (1 − Pearson correlation) were performed using Morpheus (https://software.broadinstitute.org/morpheus) (see Figure S2A).

(legend continued on next page)

phospho-p70S6K also decreased, with no change in total protein (Figure 2D; Figure S2B). Of note, we did not detect SMARCB1-dependent changes in SWI/SNF binding within 100 kB of expressed RTKs (Wang et al., 2017), nor significant changes in histone acetylation (Table S4), suggesting that reduced RTK transcript levels may not be a direct consequence of SWI/SNF binding at the RTKs, although binding to a more distal enhancer cannot be excluded.

RTK Inhibitors Suppress RTK Signaling Alone and in Combination

To relate small-molecule sensitivity data with RTK activation, we tested whether RTK inhibitors could decrease RTK phosphorylation in sensitive cell lines. As RTK inhibitors are generally ATP competitive and have overlapping target profiles, we combined available kinase profiling data (presented in Table S2) with our own cell-line-sensitivity data in non-RT CCLs harboring known activating mutations in RTKs to nominate the most likely relevant cellular target(s) of these molecules (Figure S1D). Combining these results, along with the clustering of inhibitors with shared targets (Figure 1B), suggested that these inhibitors were working via the targets identified by gene-knockout and genomic data (Figures 2A and 2B). In NCIH2004RT, A204, G401, G402, KD, and KPMRTRY cells, treatment with PDGFR-inhibiting compounds decreased phosphorylation of PDGFR and downstream AKT (Figure 2E; Figure S2C). In KYM1, TM87, TTC549, TTC642, and MON cells, treatment with MET-inhibiting compounds decreased phosphorylation of MET, GAB1, and AKT (Figure 2F; Figure S2D). In BT12 and NCIH2004RT cells, treatment with FGFR1-inhibiting compounds decreased phosphorylation of FGFR1 as well as downstream MEK1/2 or AKT (Figure S2E). In contrast to more selective inhibitors, dual-targeting small molecules such as MET/PDGFR inhibitors (cabozantinib, foretinib, glesatinib) were more broadly active in RT cell lines, including in lines that expressed and were dependent on either or both RTKs (Figure 1B; Table S3). For example, treatment of MET- and PDGFRA-expressing TTC642 cells with the selective PDGFR inhibitor imatinib and the selective MET inhibitor SGX-523 alone reduced phosphorylation of only PDGFRA or MET, respectively, while treatment with the combination of imatinib and SGX-523 or the dual inhibitor cabozantinib decreased both MET and PDGFRA phosphorylation (Figures 3A and 3B; Figure S2D). Additionally, treatment with cabozantinib decreased p-AKT and p-MEK1/2 levels to a greater extent than PDGFR or MET inhibition alone (Figure 3B; Figure S2D). Similar patterns were observed in the TTC549 cell line (Figure S2D).

As combination treatment was more effective in reducing levels of phospho-RTKs and downstream phospho-targets, we asked whether combinations of RTK inhibitors would result in synergistic cell killing. We observed that pairwise combinations of selective inhibitors of different RTKs synergized in cell lines in which multiple RTKs were active, such as in TM87, TTC549, and TTC642 cells (FGFR and MET; Figure 3C; Figures S3A, S3B, and S3D). Consistent with a recent report that identified synergy between FGFR and PDGFR inhibition in the G402 cell line (Wong et al., 2016), we also found that combinations of FGFR and PDGFR inhibitors were strongly synergistic in G402 cells (Figure 3D; Figure S3A), as well as in A204, KD, and NCIH2004RT cells (Figure S3C), which showed dependence on both *FGFR1* and *PDGFRA/B*. These findings were specific to cell lines expressing multiple RTKs: for example, synergy between FGFR and PDGFR inhibitors was not observed in TM87, BT12, or BT16 cells that did not express activated PDGFRA or PDGFRB (Figure S3D).

RTK Inhibitors Are Active against RT Xenograft Models

Collectively, these results provide support for use of multi-targeting inhibitors or combination treatments in which multiple RTKs are active. To investigate this *in vivo*, we tested the multi-targeting RTK inhibitors lenvatinib, pazopanib, and cabozantinib in an orthotopic xenograft model of the luciferase-labeled TTC642 cell line. This cell line expresses PDGFRA, FGFR1, FGFR3, and MET. Responses were compared with both no chemotherapy and with a known active standard-of-care (SOC) treatment with combination doxorubicin and vincristine. Cabozantinib was also tested in combination with SOC. Mice were treated for four 3 week courses (Figure 4A), and mice with tumor burden greater than 20% of their body weight were removed from the study and scored as having progressive disease (PD). Mice with stable disease (SD), partial responses (PRs), and complete responses (CRs) were scored using bioluminescence as previously described (Stewart et al., 2014).

Mice given the SOC treatment survived an average of 36 days, and all came off the study because of PD (Figures 4B–4H). Mice treated with cabozantinib alone, which targets PDGFRA and MET, survived longer than those on SOC, staying on treatment an average of 61 days (Figure 4D). Combination of cabozantinib and SOC further increased survival; mice survived an average of 80 days, and three of the four mice in this arm completed the entire treatment course with tumor shrinkage indicating PR (Figures 4E–4H). Mice given lenvatinib, which targets PDGFRA and FGFR family members, also survived longer than SOC (average 75 days), and three of the seven mice showed SD or PR (Figures 4C and 4F–4H). Providing further evidence that targeted multi-RTK inhibition is beneficial, all the mice treated with pazopanib, which showed the weakest activity *in vitro* against PDGFRA- and FGFR-dependent cell lines, were removed from the study for PD by 38 days (Figures 4B and 4F–4H).

(C) Fold-change of RTK pathway genes in RNA-seq in G402 cells with empty vector (EV) versus SMARCB1 re-expression after 72 h puromycin selection; mean of two biological replicates shown. p values calculated as PPEE (posterior probability of being equally expressed) in R using rsem-run-ebseq. ns, not significant; *$p < 0.05$; **$p < 0.01$.

(D) Western blots in EV and SMARCB1 G402 cells after 72 h puromycin selection (see Figure S2B). Bar graph shows results from three biological replicates (mean + SEM). p values calculated using unpaired t test without assuming a consistent SD. ns, not significant; *$p < 0.05$; **$p < 0.01$; ***$p < 0.001$.

(E and F) Westerns blots on 3 and 12 h RTK inhibitor treatment in (E) PDGFRA-expressing NCIH2004RT cells and (F) MET-expressing TTC642 and MON cells (see Figures S2C–S2E).

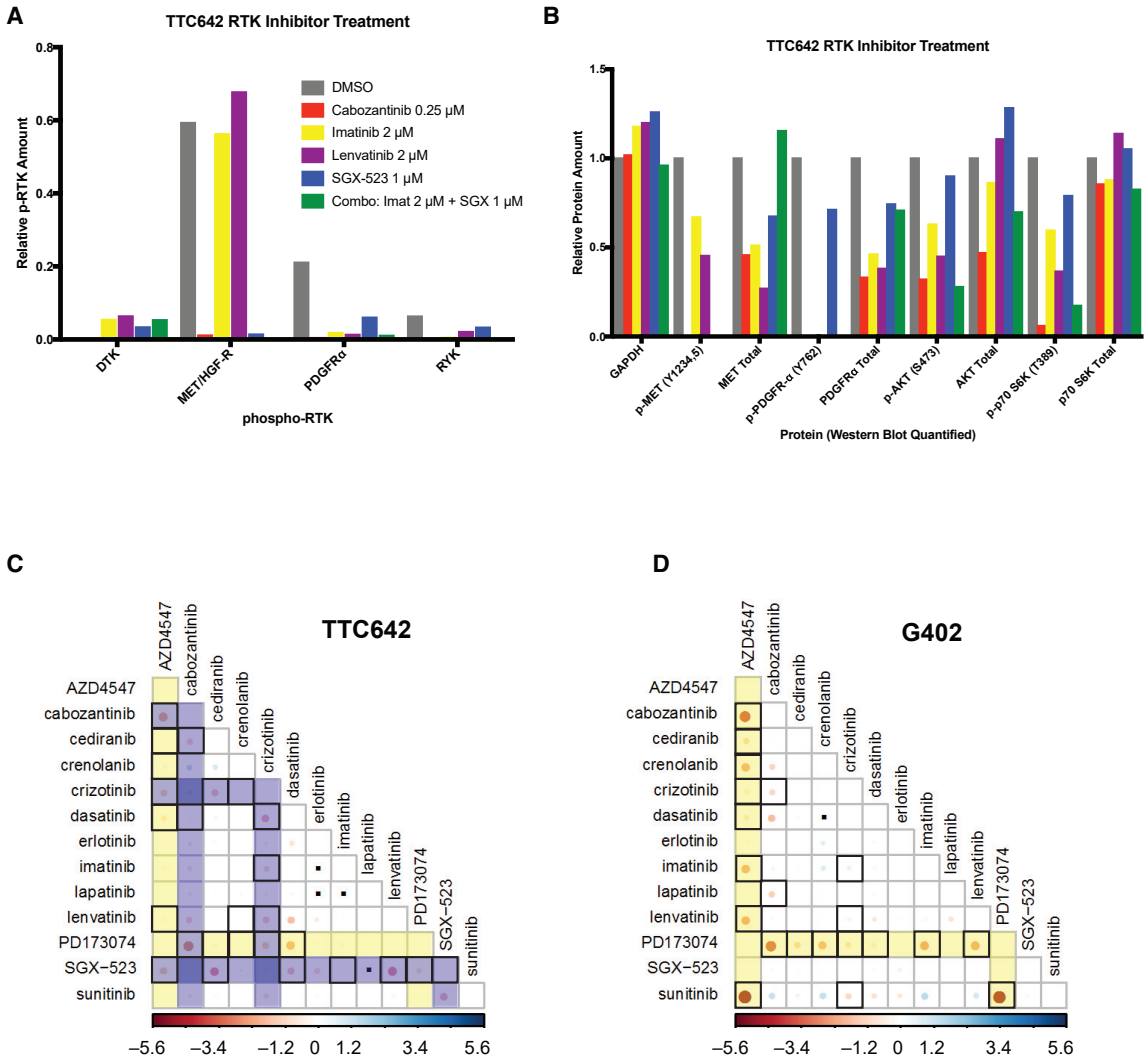

Figure 3. Combination of RTK Inhibitors Results in Synergistic Cell Killing in RT CCLs

(A) TTC642 cells were treated with indicated inhibitors for 3 h, then subjected to phospho-RTK analysis with arrays. Relative phospho-RTK expression was quantified using ImageJ (see Figure S2D).

(B) Lysates from treated TTC642 cells were run for RTK pathway members by western blot. Relative protein expression was quantified using ImageJ (see Figure S2D).

(C and D) Pairwise combination treatments of 13 RTK inhibitors in (C) TTC642 and (D) G402 CCLs. FGFR inhibitors are highlighted in yellow. MET inhibitors are highlighted in blue. Red circles indicate synergistic interactions, with interactions exceeding a 99% confidence interval threshold surrounded by a black box. Inert combinations are indicated with black dots. Visualization was performed using the Corrplot package in R (see Figure S3).

We also tested luciferase-labeled orthotopic xenografts of the FGFR1-, FGFR3-, and PDGFRA-expressing A204 rhabdoid cell line, using the same drugs and combinations, along with a combination of pazopanib and SOC. These tumors appeared more aggressive, and most mice, including those given SOC, were removed before the end of the study for PD (Figure 4H). However, three mice were able to complete the entire study, one from the lenvatinib-treatment group (CR) and two from the pazopanib and SOC group (one CR, one PR). Collectively, these results suggest that RTK inhibitor (RTKi) treatment in combination with SOC *in vivo* can provide more benefit than SOC alone and that targeting multiple RTKs may represent a more effective treatment strategy than single inhibition in tumors with multiple active RTKs.

RTK-Encoding Transcripts Show Heterogeneous Expression in RT Patient Samples

To better understand the heterogeneous nature of RTK activation and dependency in RT CCLs and its potential relevance to human RT, we collected public genome-wide expression data for 239 human RT samples across six studies, including two with samples collected from multiple tumor locations (Han et al., 2016; Chun et al., 2016), and analyzed expression of 58 human RTK genes. Across all studies, *PDGFRA*, *PDGFRB*, *FGFR1*, and *FGFR2*

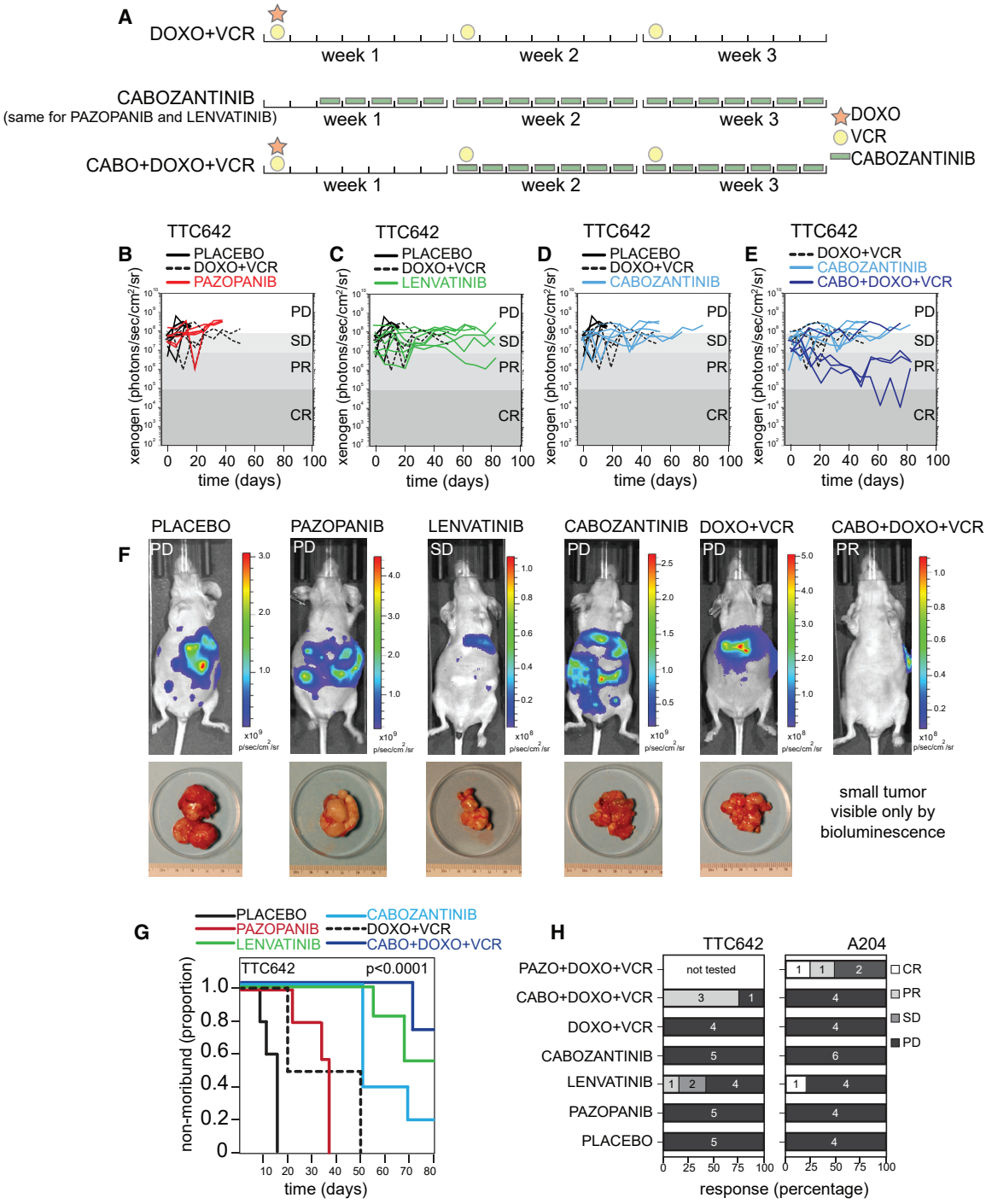

Figure 4. Preclinical Testing of Rhabdoid Orthotopic Xenografts

(A) Drug schedule selected for preclinical testing matched to relevant regimens used in patients.

(B–E) Representative plot of tumor burden for TTC642 xenografts, as measured by bioluminescence over time, in a preclinical phase 2 study with pazopanib (B), lenvatinib (C), cabozantinib (D), or cabozantinib + SOC (E) treatment groups compared with placebo control and doxorubicin + vincristine (SOC regimen used for rhabdoid tumor). Each line is a different mouse.

(F) Representative images and accompanying tumor micrographs from TTC642 xenograft mice with progressive disease in the placebo control, pazopanib, cabozantinib, and DOXO+VCR groups. Representative images of mice with stable disease in the lenvatinib group and a partial response shown for the CABO+DOXO+VCR treatment group.

(G) Survival curves for the TTC642 xenografts for the six indicated treatment groups; p value determined by log rank tests for each survival group.

(legend continued on next page)

showed the highest expression (Figure S4). However, consistent with cell-line data, we observed heterogeneity of RTK expression both within and across tissue types. For example, in the TARGET study, *PDGFRA* was more highly expressed in kidney relative to soft tissue tumors (p_{adj} = 0.0001). We also observed differential expression patterns for *MET* (highly expressed in liver samples) and *ERBB4* (highly expressed in brain relative to soft tissue; p_{adj} = 0.00167; Table S5). These findings support the importance of RTK expression in RT and are consistent with cell-line data, in which CCLs with highest phospho-PDGFRA expression were from muscle (A204) and kidney (KPMRTRY, G402, and NCIH2004RT), while ERBB4 was detected predominantly in brain-derived CCLs (e.g., BT16).

PTPN11 Represents a Shared Dependency across All RT Cell Lines

RTKs converge on canonical downstream effector proteins (e.g., AKT, MEK, S6K) that integrate signaling from multiple RTK pathways, and some mouse models of RT have been reported to show persistent AKT activation (Darr et al., 2013). Interestingly, however, the genes encoding these downstream effector proteins do not score as dependencies in CRISPR-Cas9 screening. Although most of these downstream effector proteins have functionally homologous proteins encoded by paralogous genes (e.g., AKT1/2, MAP2K1/MAP2K2, and RPS6KB1/2), potentially making any of these genes appear non-essential when singly lost, small-molecule inhibitors tend to hit all paralogs and are also not selective for RT CCLs (Figures S1A and S1E).

To more systematically investigate signaling downstream of RTKs in RT cell lines, we analyzed gene dependency scores for 476 genes within the gene ontology RTK signaling network (GO_TRANSMEMBRANE_RECEPTOR_PROTEIN_TYROSINE_KINASE_SIGNALING_PATHWAY). For each gene, we calculated the probability of dependency in each RT and non-RT cell line. Of 8 genes essential across all eight RT models (probability > 0.95), 7 were also universally essential across non-RT cell lines (minimum probability = 0.88), suggesting that these dependencies were not specific to RT cell lines or RTK signaling (e.g., components of RNA polymerase II). The exception, *PTPN11*, encodes the tyrosine phosphatase SHP2, which acts downstream of RTKs to affect survival and proliferation and is often mutated and activated in cancer.

SHP2 has been found to be an important node in RTK signaling and essential for the growth of cancers reliant on RTK signaling (Prahallad et al., 2015; Matalkah et al., 2016; Ghandi et al., 2019). Additionally, short hairpin RNA (shRNA) screening (targeting 7,500 genes) in 250 CCLs revealed that lines with activating mutations in RTKs were preferentially dependent upon *PTPN11* (encoding SHP2), and these cell lines were sensitive to a novel allosteric SHP2 inhibitor, SHP099 (Chen et al., 2016). In our genome-scale CRISPR-Cas9 screen, RT cell lines were highly dependent on *PTPN11* (dependency score range −0.96 to −1.33) (Table S6).

To determine whether rhabdoid cell lines showed preferential sensitivity to SHP2 loss, we screened the SHP099 inhibitor at eight different concentrations in 274 CCLs, including 14 RT cell lines, using PRISM, a high-throughput pooled screening assay (Yu et al., 2016). CML cell lines carrying the BCR-ABL fusion were most sensitive (Gu et al., 2018), and rhabdoid cell lines showed preferential sensitivity to SHP099 compared with other lineages (Figure 5A). Of note, RT lines had lower AUC and half maximal inhibitory concentration (IC_{50}) than cell lines containing either *PTPN11* activating mutations or RTK activating mutations. We confirmed these sensitivities across all 16 RT cell lines in conventional (unpooled) assays and observed that sensitivity to SHP099 also correlated with CRISPR-based sensitivity to *PTPN11* loss (Figure 5B; Table S6). SHP099 treatment also decreased phospho-ERK in RT cell lines and a positive control line while having no effect on a negative control line and no effect on upstream RTKs (Figure 5C; Figure S5A). Long-term (10 day) treatment also inhibited colony formation in sensitive lines while having no effect in a control insensitive line (Figure 5D). We confirmed that *PTPN11*/SHP2 is ubiquitously expressed across rhabdoid CCLs of all origins and primary human tumors (Figures S5B and S5C).

Gene Expression and Epigenetic Landscape of RT Cell Lines

Recent studies in AT/RT and RT suggest that cell lines (and tumor samples) cluster into three to four epigenetically defined subtypes, which also correlate with location of tumor origin (Torchia et al., 2015, 2016; Johann et al., 2016). In AT/RT, for example, only one of these three defined subtypes, the spinally located tumors, highly expressed and were dependent upon *PDGFRB* (Torchia et al., 2016). Therefore, we investigated whether our RT cell lines clustered into subgroups on the basis of RNA sequencing (RNA-seq) expression as well as genome-wide methylation profiling. Our collection of 16 rhabdoid cell lines are derived from tumors found in brain (AT/RT), kidney, muscle, and soft tissue. Of note, all 3 of our AT/RT cell lines have been classified as AT/RT type 2 (Torchia et al., 2016), so our findings here are limited to non-CNS and AT/RT type 2 tumors.

We performed methylation profiling and an AT/RT-defined subgroup analysis on our rhabdoid cell lines. Four lines were classified as the "MYC" subgroup, while the rest were low-confidence MYC or undefined (Table S7). Of our AT/RT lines, one was defined as low-confidence MYC and two were "undefined," making it hard to draw any conclusions. Next, we clustered CCLs on the basis of gene expression using data from CCLE, and visualized results in a t-Distributed Stochastic Neighbor Embedding (tSNE) plot. This dataset contained 1,165 CCLs, including 21 rhabdoid cell lines: the 16 rhabdoid cell lines characterized here plus 5 newly available. RT cell lines clustered closely together, indicating conserved gene expression in RT lines regardless of tissue of origin (Figure 5E). When tSNE analysis

(H) Histogram of the percentage of CR, PR, SD, and PD as determined by bioluminescence criteria for both TTC642 and A204 rhabdoid xenografts. The number of mice in each group is indicated.

CABO, cabozantinib; CR, complete response; DOXO, doxorubicin; PAZO, pazopanib; PD, progressive disease; PR, partial response; SD, stable disease; VCR, vincristine.

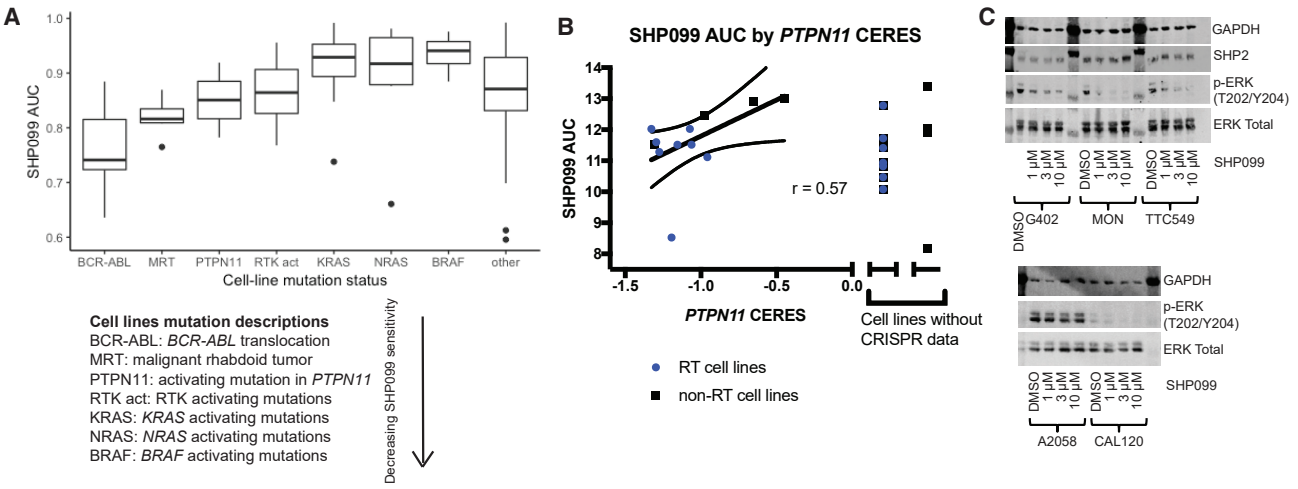

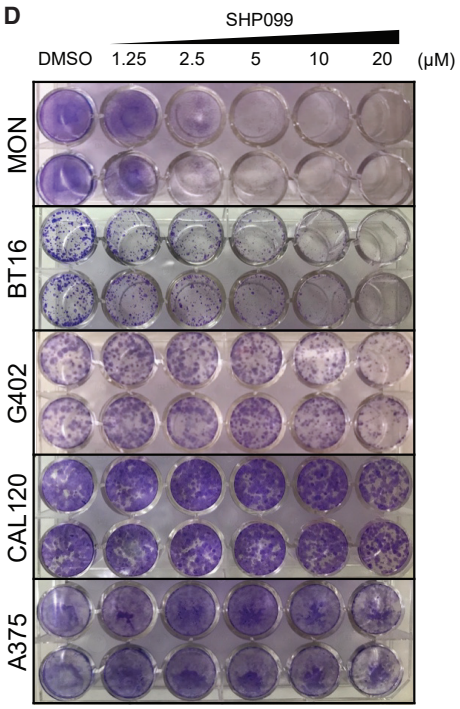

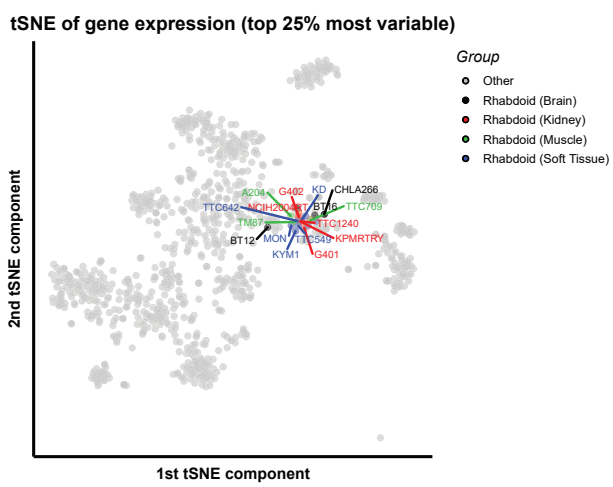

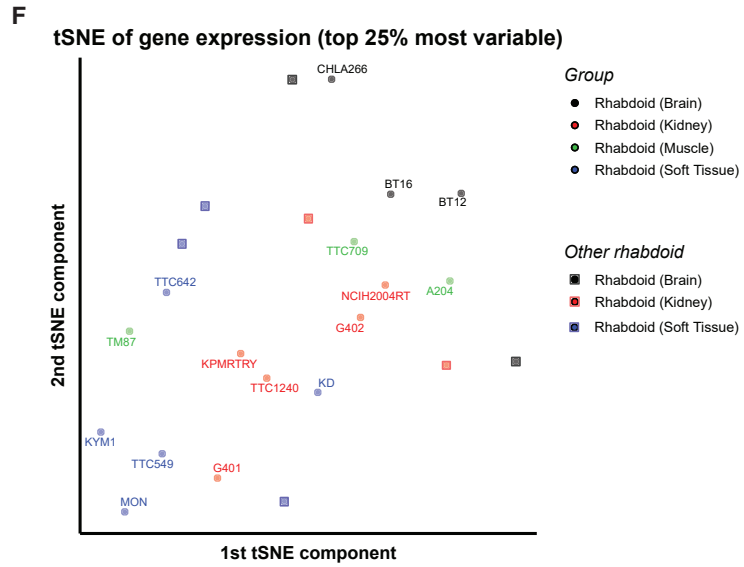

(legend on next page)

was restricted solely to RT cell lines, tissue of origin did not appear to be a major determinant of gene expression differences between lines (Figure 5F).

DISCUSSION

Pediatric RTs are driven by deletion or loss-of-function mutations in the *SMARCB1* (or rarely *SMARCA4*) tumor suppressor gene. Aside from *SMARCB1* loss, RTs have an extremely low mutation rate and an absence of recurrent mutations in other genes. Consequently, despite being one of the most aggressive and lethal cancers, there are no obvious genetically informed therapeutic targets. We therefore used RT as an exemplar to investigate whether large-scale, systematic high-throughput screening of cell lines could nominate new therapeutic approaches in the context of ''quiet'' genomes driven by loss of a tumor suppressor.

In this study, high-throughput small-molecule and genetic screening across 16 RT cell lines derived from several tissue locations was used to identify specific vulnerabilities of RT cell lines relative to cell lines representing other cancer types. These approaches converged to reveal dependencies on both RTKs and downstream SHP2 (*PTPN11*), where RT cell lines express high levels of various RTKs and are sensitive to both pharmacologic inhibition of these proteins and knockout of the genes encoding these RTKs and *PTPN11*.

Studies testing smaller numbers (n = 1–7) of RT and AT/RT cell lines have variably found activation and expression, and in some cases dependence upon, RTKs, including EGFR (Darr et al., 2015; Kuwahara et al., 2004; Chauvin et al., 2017), FGFR (Wöhrle et al., 2013; Wong et al., 2016; Chauvin et al., 2017), PDGFR (Wong et al., 2016; Torchia et al., 2016; Chauvin et al., 2017), or IGF1R (Arcaro et al., 2007), leading to uncertainty regarding the most relevant target(s). In addition to validating the known dependencies on FGFR and PDGFR, our large-scale genome-wide CRISPR-Cas9 knockout screen and follow-up screening of 30 RTKis with distinct targeting profiles enabled us to identify overexpression of and dependency on additional targets, including MET and ERBB4, in a subset of models. Our data from 16 cell lines across multiple tumor locations, combined with public tumor expression data, support the notion that RTK expression and dependency vary both within and across tissue types. The profiling of our cell lines did not seem to reliably match the published classification schema of primary tumors, conceivably a consequence of cell culture. Notably, transcriptome analysis demonstrated that regardless of tissue of origin, the gene expression profile of RT cell lines is quite similar and that the relatively limited heterogeneity between cell lines does not correlate strongly to tissue of origin, suggesting that the dependent RTKs do not constitute the greatest differential feature of the gene expression landscape.

In addition, we find that overexpression and activation of multiple RTKs is a common feature of tested RT cell lines, although it is noteworthy that the three tested AT/RT cell lines were derived from the type 2 sub-class, so we are not able to comment upon dependencies in other subtypes. RT cell lines are sensitive to appropriate single or combination treatments using existing clinically approved RTKis, but importantly, the diversity of RT models and patient samples suggests that there is no single RTKi efficacious in all RTs. Immunohistochemistry (IHC) to identify the relevant activated RTK(s) may be the most proximal marker for immediate clinical investigation. In future clinical trials, the comparison of IHC with methylation classifiers is warranted in evaluation for matching patient tumors to specific RTK dependencies.

Intriguingly, we identified a shared dependency of RT cell lines on *PTPN11*, encoding the RTK signaling effector SHP2. Recently, an analysis of results from an shRNA knockdown screen of 7,500 genes across 250 CCLs revealed that cell lines sensitive to knockdown of various RTKs were also highly sensitive to loss of *PTPN11* (Chen et al., 2016). A novel allosteric inhibitor of SHP2 was developed (SHP099) and found to be efficacious in *PTPN11*-dependent cell lines, and an optimized compound, TNO155, has entered clinical development. Although we found RT cell lines to be even more sensitive to SHP099 than cell lines with activating mutations in PTPN11 or RTKs *in vitro*, further studies (e.g., with TNO155) may inform whether SHP2 inhibition is an effective therapeutic strategy against a broader range of RT models and tumors *in vivo*.

These findings raise the question: what is the mechanistic basis by which RT are preferentially dependent upon RTKs? SWI/SNF regulates the chromatin structure at enhancers, where it facilitates transcription factor function to enable development and differentiation (Hu et al., 2011; Bossen et al., 2015; Marathe et al., 2017; Mathur et al., 2017; Wang et al., 2017; Nakayama et al., 2017). Loss of SMARCB1 in RT destabilizes the SWI/SNF complex, leading to reduced binding capacity at enhancers, which in turn results in specific reduction of the active enhancer mark H3K27ac and impaired differentiation. Restoration of SMARCB1 to RT-derived cell lines results in stabilization of the SWI/SNF complex (Wang et al., 2017) and cell-cycle arrest accompanied by expression of genes associated with

Figure 5. SHP2/PTPN11 Inhibition Is an RTK-Dependent Vulnerability Shared across RT Cell Lines

(A) Pooled cell-line screening of SHP099 at eight concentrations in 274 cancer cell lines, including 14 RT lines. Cell lines containing BCR-ABL translocation (known to sensitize to SHP2 inhibition) are the most sensitive to SHP099 (lowest AUC). RT CCLs have lower AUCs than CCLs containing RTK activating mutations (known to sensitize to SHP2 inhibition) or RAS/RAF mutations (known to create SHP2 independence).

(B) (Unpooled) validation screening SHP099 AUC (averaged across at least two replicates) correlates with CRISPR CERES scores for PTPN11 in RT cell lines and selected controls (see Figure S5A; Table S6).

(C) SHP099 treatment (3 h) decreases phospho-ERK in a concentration-dependent manner in sensitive cell lines and has no effect in negative control A2058 cells (see Figure S5A).

(D) Crystal violet staining shows that 10 day treatment of cells with SHP099 decreases number of colonies in a concentration-dependent manner in sensitive cell lines and has no effect in negative control A375 cells.

(E) Gene expression-based tSNE clustering of 1,165 cell lines reveals that rhabdoid cell lines cluster together.

(F) Clustering of 21 RT cell lines (the 16 cell lines characterized here, along with 5 more) alone does not reveal tissue-based clustering.

differentiation (Kuwahara et al., 2010; Betz et al., 2002; Mathur et al., 2017; Wang et al., 2017; Alver et al., 2017). Consequently, SMARCB1 loss may drive the growth of RT in part by preventing differentiation of highly proliferative progenitor cells in which RTKs are expressed. Here, we demonstrate that downregulation and deactivation of progenitor-active RTKs is in part dependent upon SMARCB1, as SMARCB1 re-expression results in reduced phosphorylation and expression. With respect to mechanism, this reduced activation may not be a direct consequence of altered SWI/SNF binding at the RTKs, as we did not detect SMARCB1-dependent changes in SWI/SNF binding within 100 kB of expressed RTKs, although binding to a distal enhancer cannot be excluded (Wang et al., 2017).

Together, these findings seem most consistent with the following model whereby SMARCB1 loss results in impaired enhancer function, thus "locking in" RT to the strongly RTK-driven progenitor state and precluding downregulation of RTKs that would otherwise occur with differentiation. The marked dependence of RT upon RTKs is thus a result of both gene expression related to the cell of origin combined with a functional differentiation block caused by SMARCB1 loss. These lineage-related RTK dependencies may be akin to lineage dependencies upon estrogen receptor and androgen receptor in breast and prostate cancer, respectively, both of which have shown therapeutic efficacy when targeted. As cancers driven by mutation of other SWI/SNF subunits similarly have impaired ability to activate enhancers (Wang et al., 2017; Alver et al., 2017; Mathur et al., 2017), the dependency upon RTKs could extend to the myriad other cancers in which SWI/SNF subunits are recurrently mutated, and further investigations are thus warranted.

Historically, results from preclinical testing have had modest predictive value in the outcomes of clinical trials. Although numerous factors may contribute to predictive limitations, two have been (1) concern regarding the extent to which cell-line models reflect behavior within patients and (2) heterogeneity between the cancers of different patients that is often poorly reflected in laboratory testing because of the use of only a small number of cell lines. Collectively, our work suggests that large-scale perturbational screening of CCLs uniting genetic and small-molecule approaches can be efficacious in identifying therapeutically actionable dependencies not directly encoded by an oncogenic mutation. Our work robustly validated dependencies previously predicted from analysis of primary tumors, revealed therapeutically targetable dependencies in RTs, and revealed the extent of heterogeneity in RTK dependence between cancers with remarkably simple genomes. Our findings further suggest that combination RTKi therapy, potentially coupled with profiling of expressed and active RTKs in patient tumors, and/or inhibition of SHP2, should be further investigated as potential therapies for these lethal pediatric cancers.

STAR★METHODS

Detailed methods are provided in the online version of this paper and include the following:

- KEY RESOURCES TABLE
- LEAD CONTACT AND MATERIALS AVAILABILITY
- EXPERIMENTAL MODEL AND SUBJECT DETAILS
  - Human cancer cell lines
  - Animals
  - Orthotopic Ultrasound-Guided Paranephric Xenograft Implantation
  - Preclinical Testing
  - Xenogen® Imaging
- METHOD DETAILS
  - CCL sensitivity profiling
  - Follow-up screening
  - Small-molecule combination screening
  - CRISPR screening
  - Western blotting
  - Phospho-RTK array
  - Compound treatment and protein analysis
  - Compound treatment and colony formation assay
  - SMARCB1 retroviral expression
  - RNA-seq (SMARCB1 add-back)
  - Rhabdoid cell line methylation profiling
- QUANTIFICATION AND STATISTICAL ANALYSIS
  - Xenogen® quantification and xenograft statistical analyses
  - Analysis of small-molecule combination screening
  - Western blot and phospho-RTK array quantitation
  - RNA-seq analysis
  - Rhabdoid tumor expression samples
  - Rhabdoid cell line gene expression-based clustering
- DATA AND CODE AVAILABILITY

SUPPLEMENTAL INFORMATION

Supplemental Information can be found online at https://doi.org/10.1016/j.celrep.2019.07.021.

ACKNOWLEDGMENTS

This project has been supported by grants from the National Cancer Institute: the Ruth L. Kirchstein pre-doctoral fellowship (F31 CA183558-03 to E.M.O.) and Cancer Target Discovery and Development Network grants (U01 CA176058 to W.C.H. and U01 CA176152 to S.L.S.). E.A.S is a St. Baldrick's Scholar with generous support from the Invictus Fund. This work was supported by grants R01CA172152 and R01CA113794 from the NIH to C.W.M.R. The Avalanna Fund, the Cure AT/RT Now Foundation, the Garrett B. Smith Foundation, and ALSAC/St. Jude (C.W.M.R.) provided additional support. T.R.G. and S.L.S. are investigators at the Howard Hughes Medical Institute. We would like to thank members of the Roberts lab, Schreiber lab, and Broad's Pediatric Dependencies Map Project for helpful discussion. We are also grateful to Su Wang for RNA-seq analysis guidance and Elizabeth Chun for clustering guidance and Broad's PRISM (Profiling Relative Inhibition Simultaneously in Mixture) team for screening guidance and analysis advice.

AUTHOR CONTRIBUTIONS

Conceptualization, E.M.O., M.G.R., B.S.-L., F.V., M.A.D., E.A.S., S.L.S., and C.W.M.R.; Methodology (Small-Molecule Screen), M.G.R., B.S.-L., J.H.C., A.F.S., P.A.C., and S.L.S.; Methodology (CRISPR Screen), F.V., D.E.R., T.R.G., K.S., W.C.H., and C.W.M.R.; Methodology (Mouse Work), E.A.S.; Methodology (RNA-Seq), E.M.O. and X.W.; Software and Formal Analysis (Small-Molecule Screen), E.M.O., M.G.R., B.S.-L., and P.A.C.; Software and Formal Analysis (CRISPR Screen), M.G.R., F.V., N.V.D., B.A.W., A.T., M.G., J.M.K.-B., R.M.M., P.M., and D.E.R.; Software and Formal Analysis (RNA-Seq and Molecular Subgroup Analysis), G.M.N. and N.V.D.; Software and

Formal Analysis (Methylation Profiling), S.R.; Validation, E.M.O., M.G.R., B.S.-L., F.V., J.H.C., J.M.B., and E.A.S.; Investigation, E.M.O., M.G.R., B.S.-L., X.W., J.M.B., S.R., and E.A.S.; Data Curation, M.G.R., F.V., B.A.W., A.T., J.M.K.-B., R.M.M., S.R., P.M., and P.A.C.; Writing – Original Draft, E.M.O. and M.G.R.; Writing – Review and Editing, E.M.O., M.G.R., B.S.-L., A.T., A.F.S., P.A.C., W.C.H., E.A.S., S.L.S., and C.W.M.R.; Visualization, E.M.O., M.G.R., E.A.S., and G.M.N.; Supervision, D.E.R., A.F.S., P.J.P., W.C.H., S.L.S., and C.W.M.R.; Project Administration, C.S.H., F.V., and D.E.R.; Funding Acquisition, E.M.O., M.G.R., B.S.-L., J.H.C., C.S.H., A.F.S., P.A.C., T.R.G., K.S., W.C.H., E.A.S., S.L.S., and C.W.M.R.

DECLARATION OF INTERESTS

B.A.W. is now a J&J employee. A.T. is a consultant for Tango Therapeutics. P.A.C. serves on the scientific advisory board for nference, Inc., and on a scientific advisory panel for Pfizer, Inc. T.R.G. is an advisor to GlaxoSmithKline, is a co-founder of Sherlock Biosciences, and was a co-founder and advisor to Foundation Medicine. K.S. has previously consulted for Novartis and Rigel Pharmaceuticals and has received research funding from Novartis. W.C.H. is a consultant for Thermo Fisher, AjuIB, MPM Capital, and Paraxel. W.C.H. is a founder of, holds equity in, and is a member of the scientific advisory board for KSQ Therapeutics. S.L.S. serves on the board of directors of the Genomics Institute of the Novartis Research Foundation (GNF); is a shareholder and serves on the board of directors of Jnana Therapeutics; is a shareholder of Forma Therapeutics; is a shareholder and advises Decibel Therapeutics and Eikonizo Therapeutics; serves on the scientific advisory boards of Eisai Co., Ltd., Ono Pharma Foundation, and F-Prime Capital Partners; and is a Novartis faculty scholar.

Received: July 17, 2017
Revised: April 19, 2019
Accepted: July 8, 2019
Published: August 6, 2019

REFERENCES

Aguirre, A.J., Meyers, R.M., Weir, B.A., Vazquez, F., Zhang, C.Z., Ben-David, U., Cook, A., Ha, G., Harrington, W.F., Doshi, M.B., et al. (2016). Genomic copy number dictates a gene-independent cell response to CRISPR-Cas9 targeting. Cancer Discov. *6*, 914–929.

Alver, B.H., Kim, K.H., Lu, P., Wang, X., Manchester, H.E., Wang, W., Haswell, J.R., Park, P.J., and Roberts, C.W. (2017). The SWI/SNF chromatin remodelling complex is required for maintenance of lineage specific enhancers. Nat. Commun. *8*, 14648.

Arcaro, A., Doepfner, K.T., Boller, D., Guerreiro, A.S., Shalaby, T., Jackson, S.P., Schoenwaelder, S.M., Delattre, O., Grotzer, M.A., and Fischer, B. (2007). Novel role for insulin as an autocrine growth factor for malignant brain tumour cells. Biochem. J. *406*, 57–66.

Asaoka, Y., Tada, M., Ikenoue, T., Seto, M., Imai, M., Miyabayashi, K., Yamamoto, K., Yamamoto, S., Kudo, Y., Mohri, D., et al. (2010). Gastric cancer cell line Hs746T harbors a splice site mutation of c-Met causing juxtamembrane domain deletion. Biochem. Biophys. Res. Commun. *394*, 1042–1046.

Barretina, J., Caponigro, G., Stransky, N., Venkatesan, K., Margolin, A.A., Kim, S., Wilson, C.J., Lehár, J., Kryukov, G.V., Sonkin, D., et al. (2012). The Cancer Cell Line Encyclopedia enables predictive modelling of anticancer drug sensitivity. Nature *483*, 603–607.

Betz, B.L., Strobeck, M.W., Reisman, D.N., Knudsen, E.S., and Weissman, B.E. (2002). Re-expression of hSNF5/INI1/BAF47 in pediatric tumor cells leads to G1 arrest associated with induction of p16ink4a and activation of RB. Oncogene *21*, 5193–5203.

Birks, D.K., Donson, A.M., Patel, P.R., Sufit, A., Algar, E.M., Dunham, C., Kleinschmidt-DeMasters, B.K., Handler, M.H., Vibhakar, R., and Foreman, N.K. (2013). Pediatric rhabdoid tumors of kidney and brain show many differences in gene expression but share dysregulation of cell cycle and epigenetic effector genes. Pediatr. Blood Cancer *60*, 1095–1102.

Bossen, C., Murre, C.S., Chang, A.N., Mansson, R., Rodewald, H.R., and Murre, C. (2015). The chromatin remodeler Brg1 activates enhancer repertoires to establish B cell identity and modulate cell growth. Nat. Immunol. *16*, 775–784.

Chauvin, C., Leruste, A., Tauziede-Espariat, A., Andrianteranagna, M., Surdez, D., Lescure, A., Han, Z.Y., Anthony, E., Richer, W., Baulande, S., et al. (2017). High-throughput drug screening identifies pazopanib and clofilium tosylate as promising treatments for malignant rhabdoid tumors. Cell Rep. *21*, 1737–1745.

Chen, Y.N., LaMarche, M.J., Chan, H.M., Fekkes, P., Garcia-Fortanet, J., Acker, M.G., Antonakos, B., Chen, C.H., Chen, Z., Cooke, V.G., et al. (2016). Allosteric inhibition of SHP2 phosphatase inhibits cancers driven by receptor tyrosine kinases. Nature *535*, 148–152.

Chun, H.E., Lim, E.L., Heravi-Moussavi, A., Saberi, S., Mungall, K.L., Bilenky, M., Carles, A., Tse, K., Shlafman, I., Zhu, K., et al. (2016). Genome-wide profiles of extra-cranial malignant rhabdoid tumors reveal heterogeneity and dysregulated developmental pathways. Cancer Cell *29*, 394–406.

Cowley, G.S., Weir, B.A., Vazquez, F., Tamayo, P., Scott, J.A., Rusin, S., East-Seletsky, A., Ali, L.D., Gerath, W.F., Pantel, S.E., et al. (2014). Parallel genome-scale loss of function screens in 216 cancer cell lines for the identification of context-specific genetic dependencies. Sci. Data *1*, 140035.

Darr, J., Klochendler, A., Isaac, S., and Eden, A. (2013). Loss of IGFBP7 expression and persistent AKT activation contribute to SMARCB1/Snf5-mediated tumorigenesis. Oncogene *33*, 3024–3032.

Darr, J., Klochendler, A., Isaac, S., Geiger, T., and Eden, A. (2015). Phosphoproteomic analysis reveals Smarcb1 dependent EGFR signaling in Malignant Rhabdoid tumor cells. Mol. Cancer *14*, 167.

Davis, M.I., Hunt, J.P., Herrgard, S., Ciceri, P., Wodicka, L.M., Pallares, G., Hocker, M., Treiber, D.K., and Zarrinkar, P.P. (2011). Comprehensive analysis of kinase inhibitor selectivity. Nat. Biotechnol. *29*, 1046–1051.

Gadd, S., Sredni, S.T., Huang, C.C., and Perlman, E.J.; Renal Tumor Committee of the Children's Oncology Group (2010). Rhabdoid tumor: gene expression clues to pathogenesis and potential therapeutic targets. Lab. Invest. *90*, 724–738.

Ghandi, M., Huang, F.W., Jané-Valbuena, J., Kryukov, G.V., Lo, C.C., McDonald, E.R., 3rd, Barretina, J., Gelfand, E.T., Bielski, C.M., Li, H., et al. (2019). Next-generation characterization of the Cancer Cell Line Encyclopedia. Nature *569*, 503–508.

Griffin, J.H., Leung, J., Bruner, R.J., Caligiuri, M.A., and Briesewitz, R. (2003). Discovery of a fusion kinase in EOL-1 cells and idiopathic hypereosinophilic syndrome. Proc. Natl. Acad. Sci. U S A *100*, 7830–7835.

Gu, S., Sayad, A., Chan, G., Yang, W., Lu, Z., Virtanen, C., Van Etten, R.A., and Neel, B.G. (2018). SHP2 is required for BCR-ABL1-induced hematologic neoplasia. Leukemia *32*, 203–213.

Han, Z.Y., Richer, W., Fréneaux, P., Chauvin, C., Lucchesi, C., Guillemot, D., Grison, C., Lequin, D., Pierron, G., Masliah-Planchon, J., et al. (2016). The occurrence of intracranial rhabdoid tumours in mice depends on temporal control of Smarcb1 inactivation. Nat. Commun. *7*, 10421.

Hu, G., Schones, D.E., Cui, K., Ybarra, R., Northrup, D., Tang, Q., Gattinoni, L., Restifo, N.P., Huang, S., and Zhao, K. (2011). Regulation of nucleosome landscape and transcription factor targeting at tissue-specific enhancers by BRG1. Genome Res. *21*, 1650–1658.

Iwai, M., Matsuda, M., and Iwai, Y. (2003). Cloning of a cancer cell-producing hepatocyte growth factor, vascular endothelial growth factor, and interleukin-8 from gastric cancer cells. In Vitro Cell. Dev. Biol. Anim. *39*, 288–290.

Johann, P.D., Erkek, S., Zapatka, M., Kerl, K., Buchhalter, I., Hovestadt, V., Jones, D.T.W., Sturm, D., Hermann, C., Segura Wang, M., et al. (2016). Atypical teratoid/rhabdoid tumors are comprised of three epigenetic subgroups with distinct enhancer landscapes. Cancer Cell *29*, 379–393.

Kuwahara, Y., Hosoi, H., Osone, S., Kita, M., Iehara, T., Kuroda, H., and Sugimoto, T. (2004). Antitumor activity of gefitinib in malignant rhabdoid tumor cells in vitro and in vivo. Clin. Cancer Res. *10*, 5940–5948.

Kuwahara, Y., Charboneau, A., Knudsen, E.S., and Weissman, B.E. (2010). Re-expression of hSNF5 in malignant rhabdoid tumor cell lines causes cell cycle

arrest through a p21(CIP1/WAF1)-dependent mechanism. Cancer Res. *70*, 1854–1865.

Larizza, L., Magnani, I., and Beghini, A. (2005). The Kasumi-1 cell line: a t(8;21)-kit mutant model for acute myeloid leukemia. Leuk. Lymphoma *46*, 247–255.

Lawrence, M.S., Stojanov, P., Polak, P., Kryukov, G.V., Cibulskis, K., Sivachenko, A., Carter, S.L., Stewart, C., Mermel, C.H., Roberts, S.A., et al. (2013). Mutational heterogeneity in cancer and the search for new cancer-associated genes. Nature *499*, 214–218.

Lee, R.S., Stewart, C., Carter, S.L., Ambrogio, L., Cibulskis, K., Sougnez, C., Lawrence, M.S., Auclair, D., Mora, J., Golub, T.R., et al. (2012). A remarkably simple genome underlies highly malignant pediatric rhabdoid cancers. J. Clin. Invest. *122*, 2983–2988.

Li, B., and Dewey, C.N. (2011). RSEM: accurate transcript quantification from RNA-Seq data with or without a reference genome. BMC Bioinformatics *12*, 323.

Linderman, G.C., Rachh, M., Hoskins, J.G., Steinerberger, S., and Kluger, Y. (2019). Fast interpolation-based t-SNE for improved visualization of single-cell RNA-seq data. Nat. Methods *16*, 243–245.

Liu, Y.J., Shen, D., Yin, X., Gavine, P., Zhang, T., Su, X., Zhan, P., Xu, Y., Lv, J., Qian, J., et al. (2014). HER2, MET and FGFR2 oncogenic driver alterations define distinct molecular segments for targeted therapies in gastric carcinoma. Br. J. Cancer *110*, 1169–1178.

Lorenzi, M.V., Castagnino, P., Chen, Q., Chedid, M., and Miki, T. (1997). Ligand-independent activation of fibroblast growth factor receptor-2 by carboxyl terminal alterations. Oncogene *15*, 817–826.

Love, M.I., Huber, W., and Anders, S. (2014). Moderated estimation of fold change and dispersion for RNA-seq data with DESeq2. Genome Biol. *15*, 550.

Lutterbach, B., Zeng, Q., Davis, L.J., Hatch, H., Hang, G., Kohl, N.E., Gibbs, J.B., and Pan, B.S. (2007). Lung cancer cell lines harboring MET gene amplification are dependent on Met for growth and survival. Cancer Res. *67*, 2081–2088.

Marathe, H.G., Watkins-Chow, D.E., Weider, M., Hoffmann, A., Mehta, G., Trivedi, A., Aras, S., Basuroy, T., Mehrotra, A., Bennett, D.C., et al. (2017). BRG1 interacts with SOX10 to establish the melanocyte lineage and to promote differentiation. Nucleic Acids Res. *45*, 6442–6458.

Matalkah, F., Martin, E., Zhao, H., and Agazie, Y.M. (2016). SHP2 acts both upstream and downstream of multiple receptor tyrosine kinases to promote basal-like and triple-negative breast cancer. Breast Cancer Res. *18*, 2.

Mathur, A., Ware, C., Davis, L., Gazdar, A., Pan, B.S., and Lutterbach, B. (2014). FGFR2 is amplified in the NCI-H716 colorectal cancer cell line and is required for growth and survival. PLoS ONE *9*, e98515.

Mathur, R., Alver, B.H., San Roman, A.K., Wilson, B.G., Wang, X., Agoston, A.T., Park, P.J., Shivdasani, R.A., and Roberts, C.W. (2017). ARID1A loss impairs enhancer-mediated gene regulation and drives colon cancer in mice. Nat. Genet. *49*, 296–302.

McDermott, U., Ames, R.Y., Iafrate, A.J., Maheswaran, S., Stubbs, H., Greninger, P., McCutcheon, K., Milano, R., Tam, A., Lee, D.Y., et al. (2009). Ligand-dependent platelet-derived growth factor receptor (PDGFR)-alpha activation sensitizes rare lung cancer and sarcoma cells to PDGFR kinase inhibitors. Cancer Res. *69*, 3937–3946.

Meyers, R.M., Bryan, J.G., McFarland, J.M., Weir, B.A., Sizemore, A.E., Xu, H., Dharia, N.V., Montgomery, P.G., Cowley, G.S., Pantel, S., et al. (2017). Computational correction of copy number effect improves specificity of CRISPR-Cas9 essentiality screens in cancer cells. Nat. Genet. *49*, 1779–1784.

Munoz, D.M., Cassiani, P.J., Li, L., Billy, E., Korn, J.M., Jones, M.D., Golji, J., Ruddy, D.A., Yu, K., McAllister, G., et al. (2016). CRISPR screens provide a comprehensive assessment of cancer vulnerabilities but generate false-positive hits for highly amplified genomic regions. Cancer Discov. *6*, 900–913.

Nakayama, R.T., Pulice, J.L., Valencia, A.M., McBride, M.J., McKenzie, Z.M., Gillespie, M.A., Ku, W.L., Teng, M., Cui, K., Williams, R.T., et al. (2017). SMARCB1 is required for widespread BAF complex-mediated activation of enhancers and bivalent promoters. Nat. Genet. *49*, 1613–1623.

Prahallad, A., Heynen, G.J., Germano, G., Willems, S.M., Evers, B., Vecchione, L., Gambino, V., Lieftink, C., Beijersbergen, R.L., Di Nicolantonio, F., et al. (2015). PTPN11 is a central node in intrinsic and acquired resistance to targeted cancer drugs. Cell Rep. *12*, 1978–1985.

Quentmeier, H., Reinhardt, J., Zaborski, M., and Drexler, H.G. (2003). FLT3 mutations in acute myeloid leukemia cell lines. Leukemia *17*, 120–124.

Ramos, A.H., Dutt, A., Mermel, C., Perner, S., Cho, J., Lafargue, C.J., Johnson, L.A., Stiedl, A.C., Tanaka, K.E., Bass, A.J., et al. (2009). Amplification of chromosomal segment 4q12 in non-small cell lung cancer. Cancer Biol. Ther. *8*, 2042–2050.

Rees, M.G., Seashore-Ludlow, B., Cheah, J.H., Adams, D.J., Price, E.V., Gill, S., Javaid, S., Coletti, M.E., Jones, V.L., Bodycombe, N.E., et al. (2016). Correlating chemical sensitivity and basal gene expression reveals mechanism of action. Nat. Chem. Biol. *12*, 109–116.

Ritchie, M.E., Phipson, B., Wu, D., Hu, Y., Law, C.W., Shi, W., and Smyth, G.K. (2015). limma powers differential expression analyses for RNA-sequencing and microarray studies. Nucleic Acids Res. *43*, e47.

Ritz, C., and Streibig, J.C. (2005). Bioassay analysis using R. J. Stat. Softw. *12*, 1–22.

Roberts, C.W., Galusha, S.A., McMenamin, M.E., Fletcher, C.D., and Orkin, S.H. (2000). Haploinsufficiency of Snf5 (integrase interactor 1) predisposes to malignant rhabdoid tumors in mice. Proc. Natl. Acad. Sci. U S A *97*, 13796–13800.

Ronchetti, D., Greco, A., Compasso, S., Colombo, G., Dell'Era, P., Otsuki, T., Lombardi, L., and Neri, A. (2001). Deregulated FGFR3 mutants in multiple myeloma cell lines with t(4;14): comparative analysis of Y373C, K650E and the novel G384D mutations. Oncogene *20*, 3553–3562.

Seashore-Ludlow, B., Rees, M.G., Cheah, J.H., Cokol, M., Price, E.V., Coletti, M.E., Jones, V., Bodycombe, N.E., Soule, C.K., Gould, J., et al. (2015). Harnessing connectivity in a large-scale small-molecule sensitivity dataset. Cancer Discov. *5*, 1210–1223.

Shi, W., Oshlack, A., and Smyth, G.K. (2010). Optimizing the noise versus bias trade-off for Illumina whole genome expression BeadChips. Nucleic Acids Res. *38*, e204.

Stewart, E., Goshorn, R., Bradley, C., Griffiths, L.M., Benavente, C., Twarog, N.R., Miller, G.M., Caufield, W., Freeman, B.B., 3rd, Bahrami, A., et al. (2014). Targeting the DNA repair pathway in Ewing sarcoma. Cell Rep. *9*, 829–841.

Tomlinson, D.C., Lamont, F.R., Shnyder, S.D., and Knowles, M.A. (2009). Fibroblast growth factor receptor 1 promotes proliferation and survival via activation of the mitogen-activated protein kinase pathway in bladder cancer. Cancer Res. *69*, 4613–4620.

Torchia, J., Picard, D., Lafay-Cousin, L., Hawkins, C.E., Kim, S.K., Letourneau, L., Ra, Y.S., Ho, K.C., Chan, T.S., Sin-Chan, P., et al. (2015). Molecular subgroups of atypical teratoid rhabdoid tumours in children: an integrated genomic and clinicopathological analysis. Lancet Oncol. *16*, 569–582.

Torchia, J., Golbourn, B., Feng, S., Ho, K.C., Sin-Chan, P., Vasiljevic, A., Norman, J.D., Guilhamon, P., Garzia, L., Agamez, N.R., et al. (2016). Integrated (epi)-genomic analyses identify subgroup-specific therapeutic targets in CNS rhabdoid tumors. Cancer Cell *30*, 891–908.

Uitdehaag, J.C., de Roos, J.A., van Doornmalen, A.M., Prinsen, M.B., de Man, J., Tanizawa, Y., Kawase, Y., Yoshino, K., Buijsman, R.C., and Zaman, G.J. (2014). Comparison of the cancer gene targeting and biochemical selectivities of all targeted kinase inhibitors approved for clinical use. PLoS ONE *9*, e92146.

Wang, X., Sansam, C.G., Thom, C.S., Metzger, D., Evans, J.A., Nguyen, P.T., and Roberts, C.W. (2009). Oncogenesis caused by loss of the SNF5 tumor suppressor is dependent on activity of BRG1, the ATPase of the SWI/SNF chromatin remodeling complex. Cancer Res. *69*, 8094–8101.

Wang, X., Lee, R.S., Alver, B.H., Haswell, J.R., Wang, S., Mieczkowski, J., Drier, Y., Gillespie, S.M., Archer, T.C., Wu, J.N., et al. (2017). SMARCB1-mediated SWI/SNF complex function is essential for enhancer regulation. Nat Genet. *49*, 289–295.

Weiss, J., Sos, M.L., Seidel, D., Peifer, M., Zander, T., Heuckmann, J.M., Ullrich, R.T., Menon, R., Maier, S., Soltermann, A., et al. (2010). Frequent and focal FGFR1 amplification associates with therapeutically tractable FGFR1 dependency in squamous cell lung cancer. Sci. Transl. Med. *2*, 62ra93.

Williams, S.V., Hurst, C.D., and Knowles, M.A. (2013). Oncogenic FGFR3 gene fusions in bladder cancer. Hum. Mol. Genet. *22*, 795–803.

Wöhrle, S., Weiss, A., Ito, M., Kauffmann, A., Murakami, M., Jagani, Z., Thuery, A., Bauer-Probst, B., Reimann, F., Stamm, C., et al. (2013). Fibroblast growth factor receptors as novel therapeutic targets in SNF5-deleted malignant rhabdoid tumors. PLoS ONE *8*, e77652.

Wong, J.P., Todd, J.R., Finetti, M.A., McCarthy, F., Broncel, M., Vyse, S., Luczynski, M.T., Crosier, S., Ryall, K.A., Holmes, K., et al. (2016). Dual targeting of PDGFRα and FGFR1 displays synergistic efficacy in malignant rhabdoid tumors. Cell Rep. *17*, 1265–1275.

Yu, C., Mannan, A.M., Yvone, G.M., Ross, K.N., Zhang, Y.L., Marton, M.A., Taylor, B.R., Crenshaw, A., Gould, J.Z., Tamayo, P., et al. (2016). High-throughput identification of genotype-specific cancer vulnerabilities in mixtures of barcoded tumor cell lines. Nat. Biotechnol. *34*, 419–423.

STAR★METHODS

KEY RESOURCES TABLE

REAGENT or RESOURCE	SOURCE	IDENTIFIER
Antibodies		
B-actin Rabbit mAb (HRP Conjugate)	Cell Signaling	Cat#5125; RRID: AB_1903890
CoxIV (3E11)	Cell Signaling	Cat#4850; RRID: AB_2085424
Hsp90	Cell Signaling	Cat#4874S; RRID: AB_2121214
GAPDH (14C10)	Cell Signaling	Cat#2118; RRID: AB_561053
GAPDH (D4C6R)	Cell Signaling	Cat#97166S; RRID: AB_2756824
SMARCB1/SNF5	Bethyl	Cat#A301-087; RRID: AB_2779664
p-PDGFRα (Tyr754) (23B2)	Cell Signaling	Cat#2992; RRID: AB_390728
p-PDGFRα (Tyr762)	Cell Signaling	Cat#12022; RRID: AB_2636868
PDGFRα	Cell Signaling	Cat#3164; RRID: AB_2162351
p-PDGFRβ (Tyr751)	Cell Signaling	Cat#3161; RRID: AB_331053
PDGFRβ	Cell Signaling	Cat#3162; RRID: AB_331111
VEGFR1 (clone Y103)	Abcam	Cat#ab32152; RRID: AB_778798
VEGFR2	Cell Signaling	Cat#2479; RRID: AB_2212507
p-Gab1 (Tyr307)	Cell Signaling	Cat#3234; RRID: AB_2221302
Gab1	Cell Signaling	Cat#3232; RRID: AB_2304999
p-Met (Tyr1003) (13D11)	Cell Signaling	Cat#3135; RRID: AB_2285325
p-MET (Tyr1234/1235) (D26) XP	Cell Signaling	Cat#3077; RRID: AB_2143884
p-MET (Tyr1349) (130H2)	Cell Signaling	Cat#3133; RRID: AB_2181539
Met (D1C2) XP	Cell Signaling	Cat#8198; RRID: AB_10858224
p-EGFR (Tyr1068) D7A5 XP	Cell Signaling	Cat#3777; RRID: AB_2096270
p-EGFR (Tyr992)	Cell Signaling	Cat#2235; RRID: AB_331708
p-EGFR (Tyr1045)	Cell Signaling	Cat#2237; RRID: AB_331710
EGFR	Cell Signaling	Cat#4267; RRID: AB_2246311
p-FGFR1 (Tyr653/654)	Cell Signaling	Cat#3471; RRID: AB_331072
FGFR1 (D8E4)	Cell Signaling	Cat#9740; RRID: AB_11178519
FGFR2 (Bek, C-17)	Santa Cruz	Cat#sc-122; RRID: AB_631509
FGFR3	Cell Signaling	Cat#4574; RRID: AB_2246903
p-FRS2-alpha (Tyr436)	Cell Signaling	Cat#3861; RRID: AB_2231950
p-AKT (Thr308)	Cell Signaling	Cat#9275; RRID: AB_329828
p-AKT (Ser473)	Cell Signaling	Cat#9271S; RRID: AB_329825
AKT	Cell Signaling	Cat#9272; RRID: AB_329827
p-MEK1/2 (Ser217/221)	Cell Signaling	Cat#9154P; RRID: AB_2138017
MEK1/2	Cell Signaling	Cat#9122; RRID: AB_823567
p-p70 S6K (Thr389) (108D2)	Cell Signaling	Cat#9234; RRID: AB_2269803
p70 S6K (49D7)	Cell Signaling	Cat#2708; RRID: AB_390722
SHP2 (SH_PTP2) (B-1)	Santa Cruz	Cat#sc-7384; RRID: AB_628252
Phospho-p44/42 MAPK (Erk1/2) (Thr202/Tyr204) (197G2)	Cell Signaling	Cat#4377T; RRID: AB_331775
p44/42 MAPK (Erk1/2) (137F5)	Cell Signaling	Cat#4695; RRID: AB_390779
Anti-mouse IgG Antibody, HRP-conjugated secondary	Cell Signaling	Cat#7076; RRID: AB_330924
Anti-rabbit IgG Antibody, HRP-conjugated secondary	Cell Signaling	Cat#7074; RRID: AB_2099233

(*Continued on next page*)

Continued

REAGENT or RESOURCE	SOURCE	IDENTIFIER
Goat Anti-Mouse IgG Antibody, IRDye 680RD Conjugated	LI-COR Biosciences	Cat#926-68070; RRID: AB_10956588
Goat Anti-Rabbit IgG Antibody, IRDye 800CW Conjugated	LI-COR Biosciences	Cat#926-32211; RRID: AB_621843
Chemicals, Peptides, and Recombinant Proteins		
CellTiter-Glo Luminescent Cell Viability Assay	Promega	Cat#G7573
Protease/Phosphatase Inhibitor Cocktail	Cell Signaling	Cat#5872
Halt Protease Inhibitor Cocktail	Thermo	Cat#78425
2-mercaptoethanol	Sigma-Aldrich	Cat# M6250; CAS Number: 60-24-2
TRIzol Reagent	Life Technologies	Cat#15596018
cabozantinib (gene name of protein targets: FLT3;KDR;MET;RET)	SelleckChem	S1119; CAS: 849217-68-1
dasatinib (EPHA2;KIT;LCK;SRC;YES1)	SelleckChem	S1021; CAS: 302962-49-8
Nintedanib (FGFR1;FGFR2;FGFR3; FLT1;FLT3;KDR; PDGFRA;PDGFRB)	SelleckChem	S1363; CAS: 228559-41-9
Ki8751 (KDR;KIT;PDGFRA)	SelleckChem	S1363; CAS: 228559-41-9
sunitinib (FLT1;FLT3;KDR;KIT;PDGFRA; PDGFRB)	SelleckChem	S1042; CAS: 341031-54-7
lenvatinib (FLT1;FLT3;KDR;KIT;PDGFRA; PDGFRB)	SelleckChem	S1164; CAS: 417716-92-8
axitinib (FLT1;FLT3;KDR;KIT;PDGFRA; PDGFRB)	SelleckChem	S1005; CAS: 319460-85-0
AZD4547 (FGFR1;FGFR2;FGFR3)	SelleckChem	S2801; CAS: 1035270-39-3
OSI-930 (KDR;KIT)	SelleckChem	S1220; CAS: 728033-96-3
KW-2449 (AURKA;FLT3)	SelleckChem	S2158; CAS: 1000669-72-6
SGX-523 (MET)	SelleckChem	S1112; CAS: 1022150-57-7
lapatinib (EGFR;ERBB2)	SelleckChem	S1028; CAS: 388082-77-7
foretinib (KDR;MET)	SelleckChem	S1111; CAS: 849217-64-7
quizartinib (FLT3)	SelleckChem	S1526; CAS: 950769-58-1
imatinib (ABL1;BCR;KIT)	SelleckChem	S2475; CAS: 152459-95-5
infigratinib (FGFR1;FGFR2;FGFR3)	SelleckChem	S2183; CAS: 872511-34-7
tandutinib (FLT3;KIT)	SelleckChem	S1043; CAS: 387867-13-2
cediranib (FLT1;FLT4;KDR)	SelleckChem	S1017; CAS: 288383-20-0
crizotinib (ALK;MET)	SelleckChem	S1068; CAS: 877399-52-5
pazopanib (FLT1;FLT3;KDR;KIT;PDGFRB)	SelleckChem	S1035; CAS: 635702-64-6
erlotinib (EGFR;ERBB2)	SelleckChem	S1023; CAS: 183319-69-9
tivozanib (FLT1;FLT3;KDR)	SelleckChem	S1207; CAS: 475108-18-0
glesatinib (FLT1;FLT3;KDR;MET)	SelleckChem	S1361; CAS: 875337-44-3
allitinib (EGFR;ERBB2;ERBB4)	SelleckChem	S2185; CAS: 1050500-29-2
vandetanib (EGFR;KDR)	SelleckChem	S1046; CAS: 443913-73-3
PD173074 (FGFR1;FGFR2;FGFR3;KDR)	SelleckChem	S1264; CAS: 219580-11-7
CP-673451 (PDGFRA;PDGFRB)	SelleckChem	S1536; CAS: 343787-29-1
crenolanib (PDGFRA;PDGFRB;FLT3)	SelleckChem	S2730; CAS: 670220-88-9
masitinib (KIT;PDGFRA;PDGFRB)	SelleckChem	S1064; CAS: 790299-79-5
ponatinib (ABL1;PDGFRA;KDR;FGFR1;SRC;KIT)	SelleckChem	S1490; CAS: 943319-70-8
SHP099 (PTPN11)	MedChemExpress	HY-100388; CAS: 1801747-42-1
Critical Commercial Assays		
Human Phospho-RTK Array	R&D Systems	Cat# ARY001B;

(*Continued on next page*)

Continued

REAGENT or RESOURCE	SOURCE	IDENTIFIER
DNeasy Blood and Tissue Kit	QIAGEN	Cat#69504
RNeasy MinElute Cleanup Kit	QIAGEN	Cat#74204
TruSeq Total RNA Sample Prep Kit	Illumina	Cat# 20020597
Deposited Data		
Dose-response curves from 30 RTK inhibitors across 16 RT cell lines	This paper	https://doi.org/10.17632/2vcpns9jgw.1
Density plots of AUC values of AKT and MEK inhibitors	This paper	https://doi.org/10.17632/2vcpns9jgw.1
Association of RTK dependencies and RTK transcript expression	This paper	https://doi.org/10.17632/2vcpns9jgw.1
Activity of RTK inhibitors in select non-RT CCLs	This paper	https://doi.org/10.17632/2vcpns9jgw.1
Scans of phospho-RTK arrays	This paper	https://doi.org/10.17632/2vcpns9jgw.1
Dose-response curves of pairwise combination treatments of RTK inhibitors in RT cell lines	This paper	https://doi.org/10.17632/2vcpns9jgw.1
Experimental Models: Cell Lines		
A204 (Sex: F)	Broad Biological Samples Platform (BSP)	RRID: CVCL_1058
BT12 (F)	Roberts Lab	RRID: CVCL_M155
BT16 (Sex: M)	Roberts Lab	RRID: CVCL_M156
CHLA266 (F)	Roberts Lab	RRID: CVCL_M149
G401 (M)	BSP	RRID: CVCL_0270
G402 (F)	BSP	RRID: CVCL_1221
KD (F)	Franck Bourdeaut	RRID: CVCL_U757
KPMRTRY (M)	Yasumichi Kuwahara	RRID: CVCL_7051
KYM1 (F)	BSP	RRID: CVCL_3007
MON (F)	Franck Bourdeaut	RRID: CVCL_M846
NCIH2004RT (M)	Roberts Lab	RRID: CVCL_U759
TM87 (M)	Roberts Lab	RRID: CVCL_8001
TTC549 (F)	Roberts Lab	RRID: CVCL_8005
TTC642 (M)	Roberts Lab	RRID: CVCL_8006
TTC709 (M)	Roberts Lab	RRID: CVCL_8007
TTC1240 (F)	Timothy Triche	RRID: CVCL_8002
A375 (F)	BSP	RRID: CVCL_0132
A673 (F)	Stegmaier Lab	RRID: CVCL_0080
A2058 (M)	ATCC	RRID: CVCL_1059
CAL120 (F)	BSP	RRID: CVCL_1104
LUDLU1 (M)	BSP	RRID: CVCL_2582
MeWo (M)	BSP	RRID: CVCL_0445
MKN45 (F)	BSP	RRID: CVCL_0434
MV411 (M)	BSP	RRID: CVCL_0064
T47D (F)	BSP	RRID: CVCL_0042
U2OS (F)	BSP	RRID: CVCL_0042
HEK293T (F)	ATCC	RRID: CVCL_0063
Experimental Models: Organisms/Strains		
Athymic nude immunodeficient mice	Jackson Laboratories	Strain code 007850
Recombinant DNA		
pBabe/FL-SMARCB1	Robert Kingston	N/A

(*Continued on next page*)

Continued

REAGENT or RESOURCE	SOURCE	IDENTIFIER
pBabe/Empty Vector	Robert Kingston	N/A
pCL-10A1 Retrovirus Packaging Vector	Wöhrle et al., 2013; Novus Biologicals	Cat# NBP2-29542
Software and Algorithms		
ImageJ v1.50i	NIH	https://imagej.nih.gov/ij/; RRID:SCR_003070
Prism 8	GraphPad	http://www.graphpad.com/
Spotfire v7.0.1	TIBCO	http://www.tibco.com
MATLAB R2018a	Mathworks	http://www.mathworks.com
CTRPv2.0 MATLAB curve-fitting procedures	Rees M.G., Seashore-Ludlow B., Clemons P.A. (2019) Computational Analyses Connect Small-Molecule Sensitivity to Cellular Features Using Large Panels of Cancer Cell Lines. In: Ziegler S., Waldmann H. (eds) Systems Chemical Biology. Methods in Molecular Biology, vol 1888. Humana Press, New York, NY	https://doi.org/10.1007/978-1-4939-8891-4_14; https://github.com/remontoire-pac/ctrp-reference
R v3.6	R Foundation for Statistical Computing	https://www.r-project.org/foundation/
RSEM v1.3.0	Li and Dewey, 2011	N/A
'Fit-SNE' R package for t-SNE visualization	Linderman et al., 2019	N/A
'DESeq2' R package v1.24.0 for differential expression	Love et al., 2014	N/A
'limma' R package v3.40.2 for mRNA expression processing	Shi et al., 2010	N/A
'drc' package v3.0-1 for curve fitting	Ritz and Streibig, 2005	N/A
Brain Tumor Methylation Profiler v11b4 version 2.0	DKFZ	https://www.molecularneuropathology.org
Other		
NuPAGE 4-12% Bis-Tris Protein Gels, 1.0 mm, 17-well	Thermo Fisher Scientific	Cat# NP0329BOX
Bolt 4–12% Bis-Tris Plus gels	Life Technologies	Cat# NW04120BOX
PVDF membrane	EMD Millipore	Cat# IPVH00010
Li-Cor Odyssey buffer TBS-T	LICOR	Cat# 927
HyBlot CL film	Denville Scientific	Cat# E3012

LEAD CONTACT AND MATERIALS AVAILABILITY

Further information and requests for resources and reagents should be directed to and will be fulfilled by the Lead Contact, Charles Roberts (Charles.Roberts@stjude.org). This study did not generate new unique reagents.

EXPERIMENTAL MODEL AND SUBJECT DETAILS

Human cancer cell lines

Cell lines were *Mycoplasma* negative, and identities were validated by SNP fingerprinting as described previously (Rees et al., 2016; Seashore-Ludlow et al., 2015; Cowley et al., 2014). A204, A375, CAL120, G401, G402, HEK293T, KYM1, LUDLU1, MeWo, MKN45, MV411, T47D, and U2OS cell lines were obtained from the Broad Biological Samples Platform. A2058 were ordered from ATCC. BT12, BT16, CHLA-266, NCIH2004RT, TM87, TTC549, TTC642, and TTC709 cells were maintained in the Roberts lab. A673 were maintained in the Stegmaier lab. KD and MON were a kind gift from Franck Bourdeaut at the Curie Institute. KP-MRT-RY was a kind gift from Yasumichi Kuwahara at the Kyoto Prefectural University of Medicine. TTC1240 was a kind gift from Timothy Triche at UCLA. Abbreviations: FBS, Fetal Bovine Serum; P/S, Penicillin Streptomycin. Cells were grown in a 37°C incubator with 5% CO_2.

A204 (muscle RT), G401 (kidney RT), and G402 (kidney RT) were grown in McCoy's 5A + 10% FBS + 1% P/S.

BT12 (AT/RT) were grown in OptiMEM + 5% FBS + 1% P/S.

BT16 (AT/RT), TM87 (muscle RT), A673 (Ewings), A2058 (melanoma), CAL120 (breast cancer), U2OS (osteosarcoma), and HEK293T (immortalized kidney) were grown in DMEM + 10% FBS + 1% P/S.

CHLA266 (AT/RT) were grown in IMDM + 20% FBS + 1% P/S + 1% ITS (Insulin, Transferrin, Selenium).

KYM1 (soft tissue RT) were grown in DMEM-F12 + 10% FBS + 1% P/S.

MV411 (AML) were grown in IMDM + 10% FBS + 1% P/S.

KD (soft tissue RT), KPMRTRY (kidney RT), MON (soft tissue RT), NCIH20004RT (kidney RT), TTC549 (extra-renal RT), TTC642 (extra-renal RT), TTC709 (muscle RT), TTC1240 (kidney RT), A375 (melanoma), LUDLU1 (lung cancer), MeWo (melanoma), MKN45 (stomach cancer), and T47D (breast cancer) were grown in RPMI + 10% FBS + 1% P/S.

Animals

Athymic nude immunodeficient female mice were purchased from Jackson Laboratories (strain code 007850). This study was carried out in strict accordance with the recommendations in the Guide to Care and Use of Laboratory Animals of the National Institutes of Health. The protocol was approved by the Institutional Animal Care and Use Committee at St. Jude Children's Research Hospital. All efforts were made to minimize suffering. All mice were housed in accordance with approved IACUC protocols. Animals were housed on a 12-12 light cycle and provided food and water *ad libitum*.

Orthotopic Ultrasound-Guided Paranephric Xenograft Implantation

Orthotopic rhabdoid xenografts were created by injecting luciferase-labeled A204 and TTC642 cells into recipient athymic nude mice in the paranephric location. All ultrasound procedures were performed using the VEVO 2100 high-frequency ultrasound equipped with a MS-550S transducer running at 40 MHz. A204 and TTC642 cells were grown by routine culture methods. Each cell line was suspended in Matrigel (BD Worldwide, Cat#354234) at a concentration of 1×10^5 cells per microliter and placed on ice. Anesthetized (isoflurane 1.5% in O_2 delivered at 2 l/min) recipient nude mice were placed laterally on the imaging bed such that the left flank faced upward. In order to provide a channel for delivery of the implant, a 22 gauge catheter (BD Worldwide, Cat# 381423) was gently inserted through the skin and back muscle into the paranephric region and the hub was removed. A chilled Hamilton syringe fitted with a 27 gauge needle (1.5 inch) and loaded with 10 μl of the cell suspension was guided stereo-tactically through the catheter and positioned between the kidney and adrenal gland as visualized using ultrasound. The cells were injected into the region and the needle was left in place for 30 s to permit the matrigel component to set. The needle was then slowly removed, followed by gentle removal of the catheter.

Preclinical Testing

Mice with rhabdoid orthotopic xenografts generated as described above were screened weekly by Xenogen® and the bioluminescence was measured. Mice were enrolled in the study after achieving a target bioluminescence signal of $10^6 - 10^7$ photons/sec/cm^2 to ensure tumor engraftment, and chemotherapy was started the following Monday.

A204

Mice (n = 31 total) were randomized to 7 treatment groups: Lenvatinib, Cabozantinib (CABO), Pazopanib (PAZO), Doxorubicin (DOXO) + Vincristine (VCR), DOXO + VCR + CABO, DOXO + VCR + PAZO, and placebo. The following doses were used:

TREATMENT GROUP	DOSING
CABOZANTINIB	30 mg/kg once daily continuous dosing days 1-21
LENVATINIB	30 mg/kg once daily continuous dosing days 1-21
PAZOPANIB	65 mg/kg twice daily continuous dosing days 1-21
DOXO + VCR (standard of care)	DOXO 3.5 mg/kg day 1, VCR 0.38 mg/kg day 8 and day 15
DOXO + VCR + CABOZANTINIB	DOXO 3.5 mg/kg day 1, VCR 0.38 mg/kg day 8 and day 15, CABO 30 mg/kg once daily on days 8-21
DOXO + VCR + PAZOPANIB	DOXO 3.5 mg/kg day 1, VCR 0.38 mg/kg day 8 and day 15, PAZO 65 mg/kg twice daily on days 8-21
PLACEBO	vehicle control (no chemotherapy)

TTC642

Mice (n = 30 total) were randomized to 6 treatment groups: Lenvatinib, Cabozantinib, Pazopanib, DOXO + VCR, DOXO + VCR + CABO, and placebo. The same doses were used as above.

Mice received 4 courses of chemotherapy (21 days per course) and bioluminescence was monitored weekly. Disease response was classified according to bioluminescence signal. Mice with a signal of 10^5 photons/sec/cm^2 or less (similar to background) were classified as complete response, 10^5-10^6 photons/sec/cm^2 as partial response, 10^7 up to 10^8 photons/sec/cm^2 (similar to enrollment signal) as stable disease, and greater than 10^8 photons/sec/cm^2 as progressive disease, as described previously

(Stewart et al., 2014). Mice with tumor burden at any time greater than 20% of body weight were also classified as progressive disease. Mice were monitored daily while receiving chemotherapy.

Xenogen® Imaging

Mice were given intraperitoneal injections of Firefly D-Luciferin (Caliper Life Sciences; 3 mg/mouse). Bioluminescent images were taken five minutes later using the IVIS® 200 imaging system. Anesthesia was administered throughout image acquisition (isoflurane 1.5% in O_2 delivered at 2 l/min).

METHOD DETAILS

CCL sensitivity profiling

Screening of 481 small molecules against 860 cancer cell lines has been described previously (Rees et al., 2016; Seashore-Ludlow et al., 2015). Briefly, CCLs were plated (500 cells/well) in their provider-recommended growth media in white, opaque tissue-culture-treated Aurora 1536-well MaKO plates (Brooks Automation) using a Multidrop Combi Reagent Dispenser (ThermoFisher). Compounds were added 24 hours after plating using an Echo 555 (Labcyte Inc.), and cellular ATP levels were assessed after 72 hours of compound treatment using CellTiterGlo (Promega) on a ViewLux Microplate Imager (PerkinElmer).

Forty-seven additional cell lines were screened and processed using the same procedure. Small molecules were tested over a 16-point concentration range (twofold dilution) in duplicate. Compounds were added 24 hours after plating and cellular ATP levels were assessed after 72 hours of treatment using CellTiterGlo (Promega). All raw and analyzed viability data, as well as cell-line and compound meta-data, are available from the NCI CTD^2 Data Portal (https://ctd2.nci.nih.gov/dataPortal/).

In all, area under concentration-response curves (AUCs) for 545 compounds across 907 CCLs were included for analysis. Where duplicate CCLs were tested, AUC values were averaged, resulting in a total of 887 unique CCLs tested. For each small molecule, the AUC ZMAD was calculated in R.

Annotation of genomic features for cell lines with RTK-activating mutations were collated from the following references, and verified by the Cancer Cell Line Encyclopedia (https://portals.broadinsti-tute.org/ccle/home) where possible: EOL1 (Griffin et al., 2003); NCIH1703 (Ramos et al., 2009); SW579 (McDermott et al., 2009); KASUMI1 (Larizza et al., 2005); MOLM13 and MV411 (Quentmeier et al., 2003); EBC1 (Lutterbach et al., 2007); SNU620 (Liu et al., 2014); HS746T (Asaoka et al., 2010); IM95 (Iwai et al., 2003); DMS114 and NCIH1581 (Weiss et al., 2010); JMSU1 and UMUC1 (Tomlinson et al., 2009); NCIH716 (Mathur et al., 2014); KATOIII and SNU16 (Lorenzi et al., 1997); KMS11 and OPM2 (Ronchetti et al., 2001); RT112 and RT4 (Williams et al., 2013). Published Kd values of binding (Davis et al., 2011) and percent inhibition at 1 mM (Uitdehaag et al., 2014) were used to determine most relevant targets and to select follow-up inhibitors for further study.

Follow-up screening

Cells were plated and screened in 384-well format as described previously (Rees et al., 2016). Briefly, cells were manually plated in white, opaque tissue-culture-treated plates (Corning) at 1000 cells/well, compounds were added (1:300 dilution) using a CyBi-Well Vario pin-transfer machine 24 hours after plating, and sensitivity was measured using CellTiterGlo 72 hours after the addition of small molecules. At least two biological replicates were done for each condition. See Key Resources Table (KRT) for small-molecule annotated targets and vendor information.

Small-molecule combination screening

Viability measurements were performed in 384-well plates as described above. A 1:1 mixture of the top concentration of individual compounds, followed by serial dilution (2-fold), was used for combinations, and compounds were added using a HP D300e Digital Printer.

CRISPR screening

Genome-scale CRISPR-Cas9 mediated screening has been described previously (Aguirre et al., 2016; Meyers et al., 2017). The GeCKO 19Q1 release, which includes an additional ten cell lines screened with the GeCKO library for a total of 43, was used (data available at the DepMap Portal: https://depmap.org/portal).

Western blotting

Western blotting was performed as previously described (Rees et al., 2016). See Key Resources Table (KRT) for antibody and reagent details. Whole-cell lysates were prepared by incubating cell pellets for 30 minutes in 1% NP-40 (Sigma-Aldrich) lysis buffer containing freshly added Protease/Phosphatase Inhibitor Cocktail (Cell Signaling Technology, #5872). After incubation, lysates were spun at 4°C, 13,000 RPM for ten minutes and supernatant collected and quantitated using BCA assay (Pierce). Proteins were prepared with 4 × sample buffer containing 5% 2-mercaptoethanol (Sigma-Aldrich) and heated to 95°C for 10 min

20 μg per sample was loaded onto Novex NuPAGE or Bolt 4%–12% Bis-Tris Plus gels (Life Technologies) for electrophoresis. For NuPAGE gels, proteins were then transferred to PVDF membranes (EMD Millipore) using NuPAGE transfer buffer (Life Technologies), blocked for 30 min in 5% milk (Labscientific) in PBS-T or Odyssey buffer TBS-T (LICOR, Prod# 927), and incubated overnight at 4°C with

primary antibody in 1% milk in PBS-T, 5% BSA (Sigma Aldrich) in PBS-T, or Odyssey buffer with 0.2% Tween 20. All primary antibodies were diluted to 1:1000, except for B-actin HRP (1:5000), Hsp90 (1:3000), SMARCB1 (1:6000), FGFR1 (1:5000), and AKT (1:2000).

After 3x5 min washes in PBST-T or TBS-T, membranes were then incubated for one hour at room temp with either LICOR antibodies and visualization, or rabbit HRP-linked secondary antibodies (Jackson ImmunoResearch Laboraties) at 1:3000 in 1% milk in PBS-T, then washed again and visualized on HyBlot CL film (Denville Scientific) using SuperSignal West Pico or Femto chemiluminescence substrate (Thermo Scientific). For Bolt gels, dry transfer and antibody incubation (secondary antibody: 1:15000) were performed as described previously (Rees et al., 2016), with visualization using the LICOR imaging system according to the manufacturer's instructions.

Three biological replicates of cells were prepared and run for each Western.

Phospho-RTK array

R&D Systems RTK Array (ARY001B) was used according to manufacturer's protocol. To analyze basal phospho-RTK levels, parental rhabdoid cell lines were seeded in T75 flasks and harvested when confluent.

For analysis of phospho-RTK levels after compound treatment, rhabdoid cell lines were seeded at 2M cells/10 cM plate for 24 hr, then treated with compounds for three hours. Lysates were prepared with Halt Protease Inhibitor Cocktail (Thermo 78425), quantified using BCA assay (Pierce) and 450 μg of protein was used per array. Arrays were detected on HyBlot CL film (Denville Scientific).

Compound treatment and protein analysis

Cells were plated at 400,000 cells/well in 6-well plates. At 24 hr, plates were treated with compounds (or DMSO) for the indicated time then harvested for western blotting. Two to three biological replicates were done for each condition.

Compound treatment and colony formation assay

Rhabdoid and control cell lines were seeded at 1,500 cells/well in 300 μL volume in 24-well plates. 24 hr after plating, DMSO or SHP099 was added to wells, with each concentration in duplicate. On day 4 of treatment, media was changed and SHP099 replenished. On day 10, cells were stained with crystal violet solution. Two biological replicates were done for each condition.

SMARCB1 retroviral expression

HEK293T cells were transfected with pBabe/FL-SMARCB1 or pBabe/Empty Vector (EV) and pCL-10A1 packaging vector, and retroviral supernatants collected and infected into G402 cells as described (Wöhrle et al., 2013). Media was changed at 24 hr after infection, and puromycin selection (5 μg/mL) was started at 48 hr after infection. After 48 hr selection, cells were plated at 2M cells/10 cM plate for another 24 hr, then scraped (72 hr total puromycin selection) and prepared for western blotting to confirm SMARCB1 re-expression and to probe RTK proteins. Three biological replicates were prepared and tested each for the empty vector (EV) and SMARCB1 add-back conditions

RNA-seq (SMARCB1 add-back)

Cells were harvested and prepared for RNA-seq as described previously (Wang et al., 2017). Two biological replicates were prepared each for the empty vector (EV) and SMARCB1 add-back conditions. On average, 22 million 75bp, single-end reads were generated for each sample.

Rhabdoid cell line methylation profiling

DNA was extracted from rhabdoid cell lines using the QIAGEN DNeasy Blood and Tissue Kit (Cat No. 69504) following manufacturer's instructions, and 500ng of DNA was submitted to the St. Jude Hartwell Center for Methylation Profiling using Illumina Infinium MethylationEPIC (850K) BeadChip arrays. iDAT files were uploaded and analyzed using the Brain Tumor Methylation Profiler v11b4 version 2.0 (https://www.molecularneuropathology.org) providing methylation classifier results for each sample.

QUANTIFICATION AND STATISTICAL ANALYSIS

Xenogen® quantification and xenograft statistical analyses

The Living Image 4.3 software (Caliper Life Sciences) was used to generate a standard region of interest (ROI) encompassing the largest tumor at maximal bioluminescence signal. The identical ROI was used to determine the average radiance (photons/s/cm^2/sr) for all xenografts. Survival curves of time to tumor progression were generated by the Kaplan-Meier method. Log-rank tests were used to compare survival curves across all treatment groups.

Analysis of small-molecule combination screening

Synergy calculations to assess deviation from Loewe additivity were carried out as described previously (Seashore-Ludlow et al., 2015) in R using the 'drc' package to fit curves and calculate EC_{50}, AUC and IC_{50} values (Ritz and Streibig, 2005). Combinations were excluded from synergy analysis when the maximal effect did not reach 0.5, precluding accurate estimation of IC_{50} values. At least two biological replicates were done for each condition.

Western blot and phospho-RTK array quantitation

Western blots were quantified in ImageJ (v1.50i, NIH) as described: (http://lukemiller.org/index.php/2010/11/analyzing-gels-and-western-blots-with-image-j/). For phospho-RTK arrays, films were scanned, converted to grayscale, and quantified in ImageJ. A region of interest (ROI) was defined around the pair of reference dots in the upper left corner of the array. Using this ROI, Grey Mean Value was measured around the reference dots. The empty gray space directly above these dots was measured as a background control. Another ROI was defined for the pair of dots for each protein, and this ROI was also used to measure nearby empty space as a background control. The value for each pair of dots was subtracted from its corresponding background measurement. This result for each protein was then divided by the result from the reference spots, to normalize expression within each array. The resultant values were then visualized using a heatmap.

RNA-seq analysis

Reads were aligned to the hg19 reference using RSEM v1.3.0 (Li and Dewey, 2011) (rsem-calculate-expression –bowtie2 –estimate-rspd –output-genome-bam). The RSEM commands, rsem-generate-data-matrix and rsem-run-ebseq, were then used to determine differentially expressed genes.

Cancer cell line RNA-seq data were obtained from the Cancer Cell Line Encyclopedia (CCLE):
https://ocg.cancer.gov/ctd2-data-project/translational-genomics-research-institute-quantified-cancer-cell-line-encyclopedia

Rhabdoid tumor expression samples

RNA-seq gene-level quantitation (count) data for 65 RT samples (Chun et al., 2016) were downloaded from the TARGET website (https://ocg.cancer.gov/programs/target) and analyzed for differential expression using the DESeq2 package in R (Love et al., 2014). Adjusted p values were calculated using Benjamini-Hochberg correction.

Microarray samples GSE70678 (Johann et al., 2016) GSE35493 (Birks et al., 2013), GSE64019 (Han et al., 2016), and GSE11482 (Gadd et al., 2010) were downloaded from GEO. Differential expression in GSE64019 was analyzed using GEO2R.

Data from Torchia et al. was provided by the study authors (Torchia et al., 2015) and processed using the *limma* R package, with normalization and background correction using the 'neqc' function (Shi et al., 2010; Ritchie et al., 2015).

Rhabdoid cell line gene expression-based clustering

TPM expression data for 57,820 genes and 1,165 cell lines generated by the DepMap project were downloaded from the DepMap Portal (https://depmap.org/portal, version 19q1; CCLE_depMap_19Q1_TPM.csv) The top 25% most variable genes were identified by those with the highest standard deviations of gene expression across all 1,165 cell lines. To visualize the data, t-Distributed Stochastic Neighbor Embedding (tSNE) was performed using the FIt-SNE R package (Linderman et al., 2019). Next, the expression dataset was subsetted to only include rhabdoid tumor lines. The 25% most variable genes within rhabdoid tumors were identified as above. Next, tSNE was performed using the FIt-SNE R package (Linderman et al., 2019).

DATA AND CODE AVAILABILITY

Code available for processing small-molecule sensitivity screening data is available at https://github.com/remontoire-pac/ctrp-reference. Code available for processing genome-scale CRISPR knockout data is available at https://github.com/cancerdatasci/. Any additional scripts or code written by the authors are available upon request from the corresponding author.

Original underlying data is available online from Mendeley Data DOI: 10.17632/2vcpns9jgw.1:

1. Concentration-response curves from 30 RTK inhibitors across 16 RT CCLs (data underlying Figure 1B).
2. AUC values of AKT and MEK inhibitors in RT and control cell lines (data underlying Figure S1A).
3. Association of RTK dependencies and RTK transcript expression (data underlying Figure 2A, related to Figures 1C and S1E).
4. Activity of RTK inhibitors in select non-RT CCLs (data underlying Figure S1D).
5. Scans of phospho-RTK arrays (data underlying Figures 2B, 3A, and 3B)
6. Concentration-response curves of pairwise combination treatments of RTK inhibitors in RT cell lines (data underlying Figures 3C and 3D).